DEVELOPMENT OF 20-MHZ PMN-PT SINGLE CRYSTAL PHASED-ARRAY ULTRASOUND TRANSDUCERS FOR BIOMEDICAL IMAGING APPLICATIONS

WONG CHI MAN

M. Phil.

The Hong Kong Polytechnic University

2017

The Hong Kong Polytechnic University

Department of Electrical Engineering

DEVELOPMENT OF 20-MHZ PMN-PT SINGLE CRYSTAL PHASED-ARRAY ULTRASOUND TRANSDUCERS FOR BIOMEDICAL IMAGING APPLICATIONS

Wong Chi Man

A thesis submitted in partial fulfillment of the requirements for

the degree of

Master of Philosophy

Dec 2016

CERTIFICATE OF ORIGINALITY

I hereby declare that this thesis is my own work and that, to the best of my knowledge and belief, it reproduces no material previously published or written, nor material that has been accepted for the award of any other degree or diploma, except where due acknowledgment has been made in the text.

(Signed)

________Wong Chi Man________(Name of student)

ABSTRACT

Ultrasound diagnostic has high potential for biomedical imaging applications including biomedical studies and clinic use. When comparing with other diagnostic tools, ultrasound transducer has its advantages such as compact, non-invasiveness and non-harmful, but the resolution of ultrasound is relatively low. In this thesis, an ultrasound transducer with high lateral and axial resolutions was developed by increasing its center frequency and -6 dB bandwidth. To achieve the goal, a high-frequency (a center frequency of 20-MHz) phased-array ultrasound transducer fabricated using an active layer of lead magnesium niobate-lead titanate (PMN-0.3PT) single crystal was developed. It should be noted that this single crystal material has not commonly used in commercial ultrasound transducers. Compared to the traditional piezoelectric ceramics, lead zirconate titanate (PZT), PMN-0.3PT is a piezoelectric single crystal with better piezoelectric properties, such as piezoelectric constant (d_{33} > 1000 pC/N), electromechanical coupling coefficient ($k_{33} \geq$ 0.8) and clamped dielectric constant ($\varepsilon_{33} \geq$ 1300). These outstanding piezoelectric parameters are beneficial to minimize the aperture size and enhance both -6 dB bandwidth and sensitivity of the transducer, respectively. Thus, the axial and lateral resolutions of phased-array transducer fabricated using the PMN-0.3PT material is expected to enhance for biomedical imaging applications.

Similar to the typical array transducer, the structure of the developed phased-array transducer has three main parts: an active layer for transmitting and receiving the acoustic pulse; a double quarter wavelength-thick matching layer for maximizing the acoustic pulse transmission efficiency; and a backing layer for absorbing the back reflected acoustic pulse to widen the -6 dB bandwidth of the transducer. The PMN-PT array was fabricated by the typical mechanical dicing method and independent electrodes were made by photolithography with wet etching. The 80 μm -thick array with a pitch of 75 μm (~1λ) and an element width of 55 μm was casted on the backing layer made by a conductive epoxy, E-solder. A flexible circuit with 64 electrode traces was aligned and adhered on the array. Besides, the double quarter wavelength matching layer, made by a mixture of aluminum oxide and epoxy for the first layer and a pure epoxy for the second layer, was also adhered on the array.

The performance of developed phased-array transducers has shown a center frequency of 22. By using the built-in FFT function of the oscilloscope, the pulse-echo response in the frequency domain illustrated a -6 dB bandwidth of 91%. The sensitivity of the phased-array transducer was represented by an insertion loss of 29 dB. Comparing with the commercial or reported array transducers within the specific high-frequency range

(20 MHz to 50 MHz), the -6 dB bandwidth of the developed array prototype is the widest and its sensitivity is also comparable. The small aperture size ((L) 5 mm × (W) 5 mm × (H) 2.2 mm) and wide -6 dB bandwidth (>70%) of the developed transducers are highly appropriate for accomplishing high-resolution imaging in the biomedical and clinical applications.

LIST OF PUBLICATIONS

Journal Publication

[1] C.-M. Wong, Y. Chen, H. Luo, J. Dai, K. H. Lam, and H. L.-W. Chan, "Development of a 20-MHz Wide-Bandwidth PMN-PT Single Crystal Phased-Array Ultrasound Transducer," Ultrasonics, vol. 73, no. C, pp. 181–186, Jan. 2017.

[2] H. J. Fang, Y. Chen, C. M. Wong, W. B. Qiu, H. L. W. Chan, J. Y. Dai, Q. Li, and Q. F. Yan, "Anodic Aluminum Oxide-Epoxy Composite Acoustic Matching Layers for Ultrasonic Transducer Application," Ultrasonics, vol. 70, no. C, pp. 29–33, Aug. 2016.

[3] Y. Chen, K. Mei, C.-M. Wong, D. Lin, H. Chan, and J. Dai, "Ultrasonic Transducer Fabricated Using Lead-Free BFO-BTO+Mn Piezoelectric 1-3 Composite," Actuators, vol. 4, no. 2, pp. 127–134, Jun. 2015.

International Conference Proceeding Publication

[1] C.-M. Wong, Y. Chen, H. Luo, J. Dai, K. H. Lam, and H. L.-W. Chan, “An Ultrawide Bandwidth High Frequency Phased-Array Ultrasound Transducer Fabricated Using the PMN-0.3PT Single Crystal,” presented at the 2016 IEEE International Ultrasonics Symposium (IUS), 2016, pp. 1–4.

Patent

[1] Jiyan Dai, H.J. Fang, Chi-Man Wong, Yan Chen, "A New Fabrication Method of 2-Dimensional Array Ultrasound Transducer for 3-Dimensional Imaging", China 105596027A, 2016.

ACKNOWLEDGEMENTS

I would like to thank Dr. Kwok Ho Lam and Prof. Jiyan Dai for their guidance and support. I was lucky to have them as my advisors because I have learned not only how to conduct research, but also more importantly how we can contribute to the world with what we can do for the better future.

I am very grateful to all our current and former group members, Dr. Yan Chen, Mr. Qi Zhang, Ms. Yongxin Lyu and Ms. Siu-Fan Chan, for their support and sharing the wonderful moments for the past few years. Also, special thanks for the senior artisan Kai-Hong Ho who made the fabulous mechanical devices and assemblies. I wish to thank Dr. Hardy Lui of the Materials Research Centre, and Dr. Terence Wong and Ms. Joyce Lau of the University Research Facility in Materials Characterization and Device Fabrication for their assistance in equipment operation.

I also would like to thank my friends, Hei-Man Yau, Chun-Hung Suen, Cheuk-Ho Chan, for their love and support. I also would like to thank my parents. In all, I would like to thank my thesis's financial support: the Hong Kong Polytechnic University (Grant Nos. 1-ZVCG, 4-ZZDC and G-YBLM) and the Hong Kong Research Grants Council (ECS

Grant No. 253001/14P). This research was also supported by the National Key Basic Research Program of China (973 Program) under Grant No.2013CB632900 and the support from Shantou Institute of Ultrasonic Instrument (No: H-ZG4S). Thanks also give to Department of Electrical Engineering and Department of Applied Physics of the Hong Kong Polytechnic University.

TABLE OF CONTENTS

LIST OF FIGURE CAPTIONS

LIST OF TABLE CAPTIONS

CHAPTER 1 INTRODUCTION

1.1 BACKGROUND

High frequency ultrasound is used currently for various imaging applications such as small animals studies [1], ophthalmology [2], [3] and dermatology [4]. In medical diagnostics, comparing to X-ray, magnetic resonance imaging (MRI) and computed tomography (CT), ultrasound diagnostic tools can be used to diagnose diseases of diverse body regions of both large- and micro-scales that are brain, liver, heart and blood vessel [5]. Although those images can be obtained by X-ray, MRI and CT, respectively, the portability, generalization and cost efficiency of those devices are low

Figure 1.1 A typical ultrasound imaging system [6].

in contrast to the ultrasound imaging system. An ultrasound transducer imaging system usually consists of three main parts that are an ultrasound transducer for ultrasound transmission and collection, a data processing system and a control system. Figure 1.1 shows the outlook of a typical ultrasound imaging system (Vevo 3100 Imaging Platform, Fujifilm VisualSonics Inc.) that is obviously smaller in size compared to other imaging systems [6]. Thus, ultrasound imaging systems are popular and transferred easily in hospitals due to its relatively small size. The compact system also benefits for assisting operations in surgery rooms. Space limitation is always a critical problem in places where lack of land resources, such as Hong Kong. The space of surgery room would limit the type or size of equipment. The ultrasound imaging systems provide a compromising solution that can offer effective diagnosis and reduce the consultation time.

For the ultrasound imaging systems, the core imaging device is the ultrasound transducer. The ultrasound transducer can be with different center frequencies or focal points to collect images from organs with different acoustic impedances in different locations (this part will be explained in Chapter 1.2.2). Thus, multiple organs can be imaged by only changing the ultrasound transducers rather than the whole system. The ultrasound diagnostic tools can acquire many types of physiological data that are not only the appearance of organs, but also the real-time blood flow speed monitoring [7], which are unable to be obtained by other diagnostic tools, such as MRI and X-ray. Besides, due to the working mechanism of ultrasound imaging systems, the cost of the system with multiple transducers is still remarkably low compared to other diagnostic tools, such as MRI, CT and X-ray. That makes the ultrasound diagnose tools become a cost-effective tool compared with others.

Besides having the advantages of compact and low cost, the ultrasound diagnostic tool is also noninvasive [8], which means the imaging process is safe to patients. Comparing with the radioactive diagnostic tool, such as X-ray may cause health damage if patients and operators are exposed under X-ray frequently, the ultrasound wave can be harmless to biomedical tissues. Thus, ultrasound can be used in pregnancy or for biomedical clinical studies without adversely affecting the observed object. Moreover, the ultrasound diagnostic tool has fewer limitation factors compared with other diagnostic tools. For example, MRI is not available for a patient who has metallic bone plates and implantable cardioverter defibrillator (ICD). Serious medical accident may be caused if human negligence was happened. Obviously, safety is a main consideration for clinic use, that is why the ultrasound diagnostic tool is commonly used to assist physicians for performing operations. The safeness of ultrasound transducer seems to be the main advantage, showing the potential for its further development.

With the above advantages, the ultrasound diagnostic tool has become one of the valuable diagnostic tools in clinic and medical studies so that it has been developed rapidly in the past decades [9]-[11]. Nowadays, only a few global companies are developing the high frequency ultrasound imaging systems, such as Fujifilm VisualSonics, Olympus and Analogic. The systems produced by those companies are fixed in a narrow range of usage and sold in high prices that are inappropriate for researchers who need an ultrasound imaging system for biomedical studies. As mentioned before, the criteria of transducer for imaging different organs are distinct, so the demand of different types of transducer is high, inducing massive cooperation chances between academic research and industry. Since the desired transducer and processing unit are with higher frequencies and novel properties in research compared to the commercial products, the main research objective is to investigate and develop transducers with the enhanced performance and higher frequencies.

When comparing with other diagnostic tools, the main disadvantage of ultrasound imaging system is its low imaging resolution. Figure 1.2 shows the images taken by MRI and ultrasound, respectively [12], [5]. The image taken by ultrasound (Figure 1.2(a)) is a typical brightness mode (B-mode) image of human kidney, which illustrates only a rough boundary of the kidney without the detailed internal structure. On the contrary, the MRI image (Figure 1.2(b)) shows the details of a mouse brain. The resolution of the MRI is obviously higher than that of the ultrasound. Therefore, the ultrasound imaging resolution enhancement is always the first priority in ultrasound diagnostic tools development.

The motivation of this project is very clear according to the above descriptions. ultrasound can become a much useful biomedical diagnostic tool if the imaging resolution is further enhanced. That is why the development of high performance ultrasound transducers is the main theme in this study.

In the following section, the structure of the ultrasound transducer, the factors influencing the resolution of ultrasound transducer, and the working mechanism of ultrasound transducer will be elaborated.

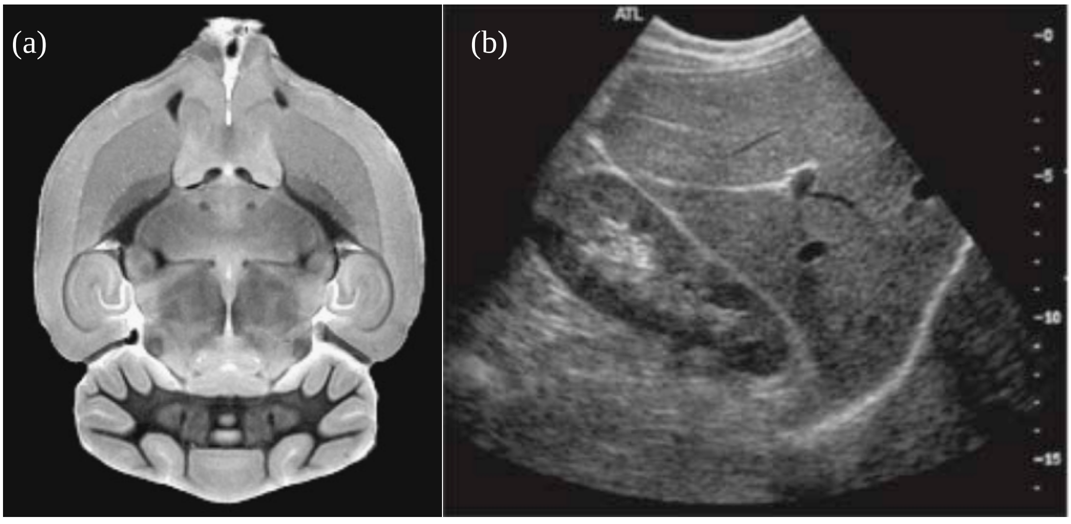

Figure 1.2 Images taken by (a) magnetic resonance imaging [12] and (b) ultrasound [5].

1.2 THEORY

1.2.1 Basic structure of ultrasound transducer

The ultrasound transducer is simply a device that transfers an electrical signal to an acoustic signal and vice versa. By transmitted an acoustic pulse and received a reflected acoustic pulse (echo) from the target, the characteristics of the received echo can be analyzed by the image processing system to produce an image represented by brightness spots in the B-mode image. Alternatively, with using different types of ultrasound transducer or different scanning methods, 2-dimensional (2-D), 3-dimensional (3-D) or even real time 3-D (4-dimensional (4-D)) imaging can be performed. In general, the ultrasound transducers consist of three main components that are active element, matching layer and backing layer. Figure 1.3 illustrates the basic structure of a typical

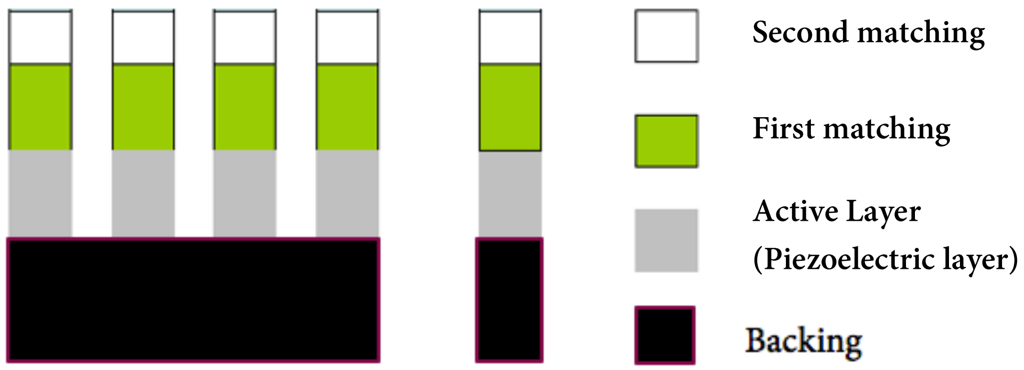

Figure 1.3 Basic structure of array Transducer with double matching layer.

array transducer. For the active layer, the material is mostly the piezoelectric material that converts an electrical signal into an acoustic signal and vice versa. The mechanism of the piezoelectric material being the active layer depends on the piezoelectric effect that an external electric field applying on the piezoelectric material redirects the dipoles inside the material, and thus a strain is generated in either the lateral direction or the longitudinal direction. Similarly, an AC electric field applying on the piezoelectric material can induce its vibration. The vibration frequency would depend on the AC electric field frequency and the intrinsic characteristics of the piezoelectric material. Consequently, the vibration of the piezoelectric material vibrates the molecules of the surrounding medium, and then generates an acoustic pulse based on the resonance frequency of the piezoelectric material, i.e. higher than 20 kHz if the piezoelectric material is thinner than 1 cm. The detailed explanation will be illustrated in Chapter 1.2.3.1.

The second component is the matching layer, which can enhance the transmission rate of the ultrasound between the active layer and the medium. The transmission rate depends on the acoustic impedance difference between the medium and the active layer. The enhanced transmission rate would increase the transmitted and received acoustic energies as well as the sensitivity of the ultrasound transducer. The further details will be described in Chapter 1.2.3.2.

The third component is the backing layer. The mechanism of the backing layer is very similar to that of the matching layer. The only difference is that the function of backing layer intends to absorb the acoustic wave propagating through the backside of the ultrasound transducer, where is the direction opposite to the target. By absorbing the backside acoustic wave, the bandwidth of the acoustic pulse emitted by the transducer becomes boarder, so the imaging resolution can be enhanced. The relationship between the resolution and the bandwidth will be explained in Chapter 1.2.2 and the details of the backing layer will be illustrated in Chapter 1.2.3.3.

1.2.2 Resolution in ultrasound transducer

The performance of the ultrasound transducer for biomedical imaging applications is determined by its sensitivity and resolution. The sensitivity is simply defined as the amplitude of the echo collected by the transducer. The resolution of the transducer is divided into two types, which are the axial resolution and lateral resolution. The axial resolution is the resolution along the ultrasound pulse propagation direction, which depends on the pulse length. The lateral resolution is related to the beam width of transducer. The spatial resolutions of transducer in three different directions are shown in Figure 1.4 [13].

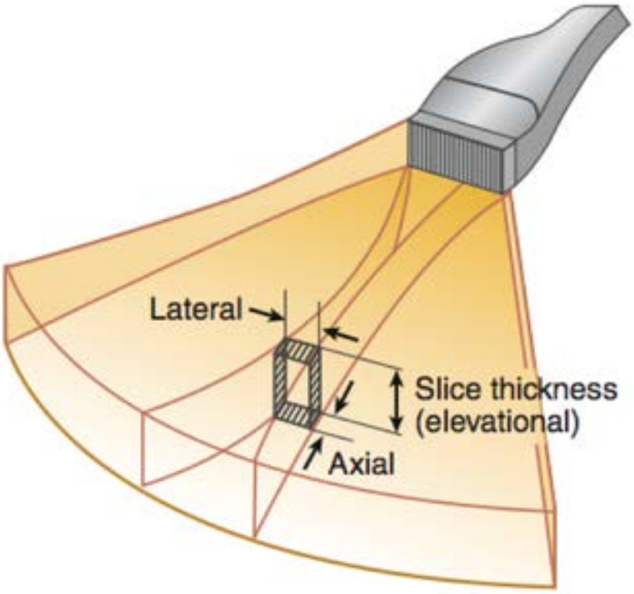

Figure 1.4 Resolution profile in 3-D imaging of array-transducer [13].

With a shorter pulse length, the echo reflected by the first object is not interfered with the echo reflected by the adjacent object that is located deeper in the axial direction of the transducer. Then, the first and the second echoes can be identified as two distinct signals and displayed in the image after signal processing.

However, the pulse length is hard to define in the time domain, so the fast Fourier transform (FFT) is applied to transform the echo signal from the time domain to the frequency domain. In the frequency domain, the pulse length is represented by the -6 dB bandwidth of the spectrum. According to the below equation, -6 dB represents the output is half of the input value, which means the signal with the amplitude lower than half of the input is not counted in the pulse length.

$$dB = -20\log(V_o / V_i) \tag{1}$$

With the FFT, the equation is listed as follows,

$$G(\omega) = \int_{-\infty}^{+\infty} g(t)e^{-j\omega t}\,dt \tag{2}$$

A single acoustic pulse is seen to be a function *g(t)* in the time domain combined by various sinusoidal waves with different periods t. $G(\omega)$ is the resultant component at a specific frequency, ω. By transferring each sinusoidal wave function from the time domain to the frequency domain, several discrete $G(\omega)$ are defined if the acoustic pulse repetition is short. In the usual excitation cases, the acoustic pulse repetition is far longer than the pulse length, thus, the function $G(\omega)$ becomes a continuous function. The width of the function in the frequency at -6 dB has an inversely proportional relationship with the acoustic pulse length. Therefore, the axial resolution of the transducer increases simultaneously with the -6 dB bandwidth, consequently, it can be determined scientifically rather than calculating the pulse length in the time domain. The following equation presents the axial resolution in term of bandwidth:

$$R_{axial} = \frac{c}{2BW} \tag{3}$$

where c is the acoustic wave velocity in the medium and BW is the -6 dB bandwidth of the transducer.

As mentioned, the lateral resolution is related to the beam width of transducer. With a narrower beam width, the resolution is considered to be increased because the adjacent objects can be determined. The beam width of the acoustic beam emitted by the transducer is defined as follows:

$$\text{Beam width} = \lambda L/D \quad (4)$$

In Eq. (4), for an unfocused transducer, λ is the wavelength of the acoustic pulse in the medium, L is the distance between the transducer and the target, D is the aperture size of the transducer. Figure 1.5 shows schematic diagrams of acoustic beams emitted by the unfocused and focused single-element transducer, respectively [13]. It is shown that

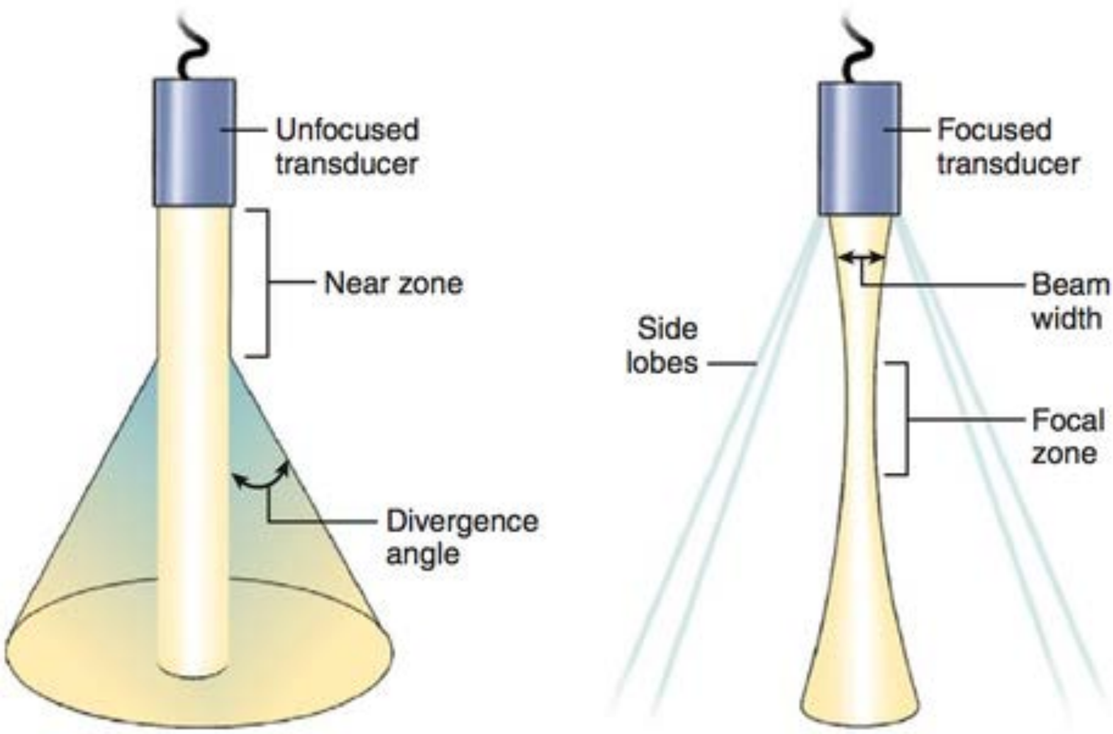

Figure 1.5 Ultrasound beam profiles of unfocused and focused single-element transduers [13]

the unfocused acoustic beam is nearly parallel (equal beam width) within the near-field zone (also called Fresnel zone), and dispersed with a certain divergence angle to the infinite distance after the near-field zone. Thus, the lateral resolution of the unfocused transducer is almost the same within the near-field zone. The resolution is the highest at the near-field far-field transition point, but it drops gradually beyond the transition point along the axial direction of the transducer. On the other hand, the focused transducer has the narrowest beam width (and so the highest resolution) in the focal zone between the near zone and far zone. Since the applicable range is narrow, the focused single-element transducers are not appropriate for medical imaging. It should be noted that array transducers would also have the similar beam profile as shown in Figure 1.5. The main difference is that the phased-array transducer has an adjustable focal point and narrower beam width.

In summary, the axial resolution of transducer is influenced by the aperture size and the center frequency, while the lateral resolution is affected by the bandwidth. By compromising the above parameters, a phased-array transducer with high imaging resolution can be designed and developed.

1.2.3 Working mechanisms of different parts in ultrasound transducer

In this section, the main factors affecting different layers of the ultrasound transducer will be described. To implement high resolution and sensitivity ultrasound transducers for biomedical imaging, it is essential to understand the working mechanisms of different components in the transducer. The factors are mainly the properties of the piezoelectric material, such as piezoelectric constants and electromechanical coupling coefficients, and the ultrasound transducer specifications depended on the design and fabrication precision.

1.2.3.1 Piezoelectric effect

The mechanism of acoustic wave generated by the piezoelectric material can be

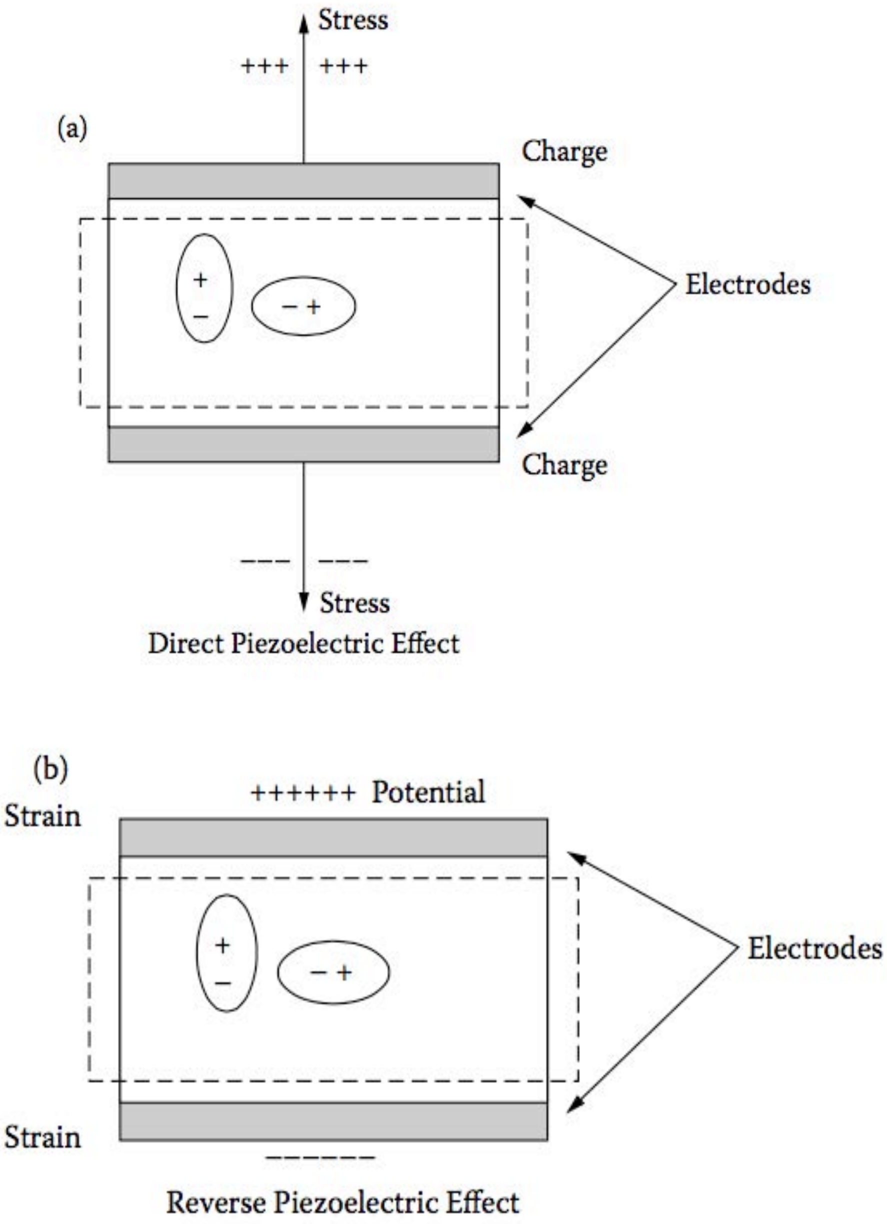

Figure 1.6 Schematic diagrams of piezoelectric effects in a piezoelectric material [8].
a) Direct piezoelectric effect: charges separation induced by an external stress. (b) Reverse piezoelectric effect: a strain induced by applying a potential difference on both sides of electrodes.

explained using the piezoelectric effect. A piezoelectric effect is a phenomenon that a material would change its physical dimensions by applying an external electric field and vice versa. Two French physicists, Pierre and Jacques Curie, discovered this effect in 1880. Figures 1.6 (a) and (b) show schematic diagrams of the piezoelectric effect [8]. The piezoelectric effect can be explained on the basis of innumerable electric dipoles inside the material. The dipoles are randomly arranged without being affected by any external source, such as an electric field, resulting in a neutral state with no net charge. The dipoles are realigned by applying a potential difference across the material surface, resulting in a deformation.

Most dipoles of the piezoelectric material could return to its original alignment after removed the external electric potential. However, some materials called ferroelectric material, which is a subset of the piezoelectric materials, can remain their dipoles aligned even after removed the potential. Figure 1.7 shows the relationships between piezoelectrics, pyroelectrics and ferroelectrics [14]. Actually, all the piezoelectrics, pyroelectrics and ferroelectrics are the dielectric material. Piezoelectrics is a material that possesses the piezoelectric effect. Pyroelectrics is a material that exhibits the phenomenon in which its charge is induced and changed against the temperature. Ferroelectrics possesses both piezoelectric and pyroelectric effects, besides, it has a property called a spontaneous polarization that is a polarization induced by the retained dipoles. The polarization of the ferroelectric material can be induced by a strong electric field at an elevated temperature. This process is called poling. The poling field depends on the material properties and dimensions, while its direction depends on the desired vibration mode.

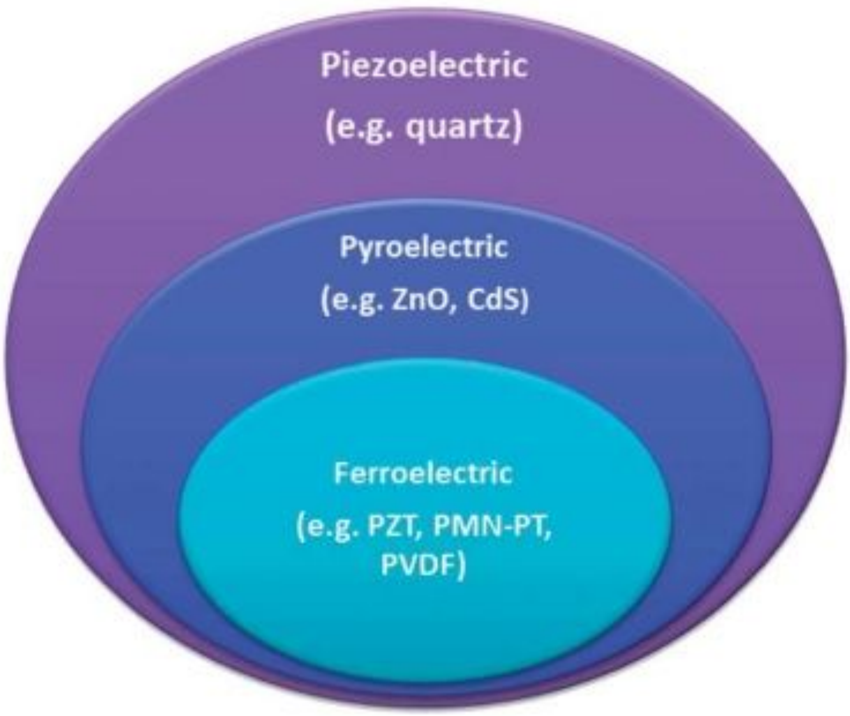

Figure 1.7 The relationship between piezoelectric, pyroelectric and ferroelectric materials [14].

Typically, the microstructure of the material determines its polarization. For example, a single crystal material, such as lead magnesium niobate - lead titanate (PMN-PT), has a uniform crystal structure that exhibits fewer defects, lower losses and no grain boundary theoretically. Thus, the dipoles of the single crystal structure can be aligned in almost the identical direction during the poling process. The net dipole vector would reach the maximum due to nearly no counteraction of dipoles inside the material. On the other hand, for the material with a polycrystalline structure, such as lead zirconate titanate (PZT), its structure contains numerous grain boundaries so that its dipole alignment is bounded by the grain direction during the poling, resulting in non-uniform dipole alignment. Dipole alignments of both single crystal and polycrystalline structures are shown in Figure 1.8 [15]. This explains why the single crystal material exhibits higher electromechanical coupling coefficients compared to the polycrystalline material.

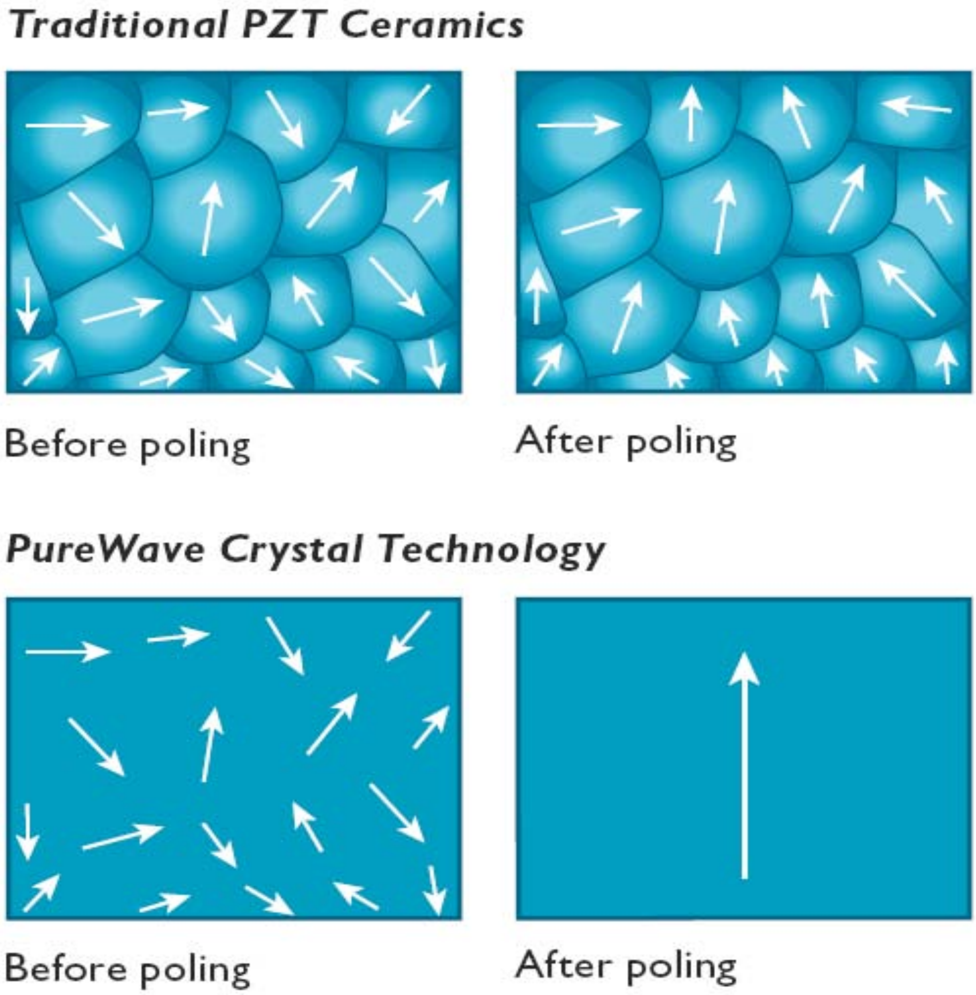

Figure 1.8 Schematic diagrams of dipoles direction of polycrystalline material and single crystal material before and after the poling process [15].

1.2.3.2 Active layer

Due to the piezoelectric effect, the piezoelectric material vibrates by applying an AC electric field at a certain frequency. The vibration turns into a pressure applying on the medium that triggers the particle displacement with a direction parallel to the pressure propagation direction, which is a longitudinal acoustic wave. The frequency of the acoustic wave is defined by the equation $v = f\lambda$, where v is the velocity of the wave in the medium, f is the frequency, and λ is the wavelength of the acoustic wave. Assume that the vibration is a wave resonance inside the material, it can only be in resonance if the thickness of the material along the electric field direction is equal to half wavelength of the resonance wave while the constructive interference occurs. The resonant frequency should be the same as the acoustic wave frequency so that, according to the velocity equation, it becomes $v/2 = f \cdot t$ when $\lambda/2 = t$, where t is the thickness of the piezoelectric active layer. The $v/2$ is called the frequency constant. Since the velocity in a medium is unchanged, the relationship of the thickness of the active layer and acoustic wave frequency can be found. With the known velocity, the wavelength of the acoustic wave in different media can be determined by the center frequency of the ultrasound transducer. Besides, the resonant frequency of ultrasound transducer can be controlled by tuning the thickness of the active layer. The center frequency of the transducer increases with reducing the thickness of the active material As most piezoelectric materials are with the longitudinal velocity larger than 4000 m/s, it is difficult to fabricate ultrahigh-frequency (≥ 100 MHz) ultrasound transducers due to the requirement of very thin active material (~20 μm). Some piezoelectric materials, such as aluminum nitride (AlN), possess very high longitudinal velocity of ~$10000\ m/s$. However, the transducers fabricated using those materials are usually weak in acoustic intensity. Besides, although the thickness of the active layer can be solved by using materials with high velocity, the further thin matching layer is still a critical challenge when the transducer frequency is high.

1.2.3.3 Matching layer

According to wave properties, the acoustic wave has reflection and refraction natures. The acoustic wave is reflected by the medium interface when it is travelling from one medium to another with either the same or different acoustic impedances. The acoustic impedance (Z) is defined as the response of the particles of the medium in terms of their velocity by giving the wave a certain pressure. The equation of the acoustic impedance is written as $Z = p / v$ where p is the pressure and v is the particle velocity. The concepts of the acoustic impedance in a medium can be explained by using a train of mass connected with a spring as shown in Figure 1.9 [5]. One of the chains has a small mass (m) connected with a soft spring (k), representing a low density and low stiffness medium while the other chain is connected with a large mass (M) and a stiff spring (K), representing a medium with high density and stiffness. The pressure applied on the upper chain can propagate along the chain with low resistance because the light mass and the particle movement within the chain in response to the given pressure is large, thus the impedance is low. On the contrary, the same pressure applied on the second chain is resisted by the stiff spring and the heavy mass so that the particle response movement is slow in the second chain, resulting in high impedance according to the definition of impedance. In this mechanical spring-mass diagram, the acoustic impedance can be represented by $Z = \sqrt{\rho k}$, where ρ is the density and k is the spring constant. By combining the equation of speed of sound, the impedance becomes:

$$Z = \rho c \tag{5}$$

where c is the speed of acoustic wave. Table 1.1 lists the acoustic properties of different mediums including biological materials and non-biological materials [16].

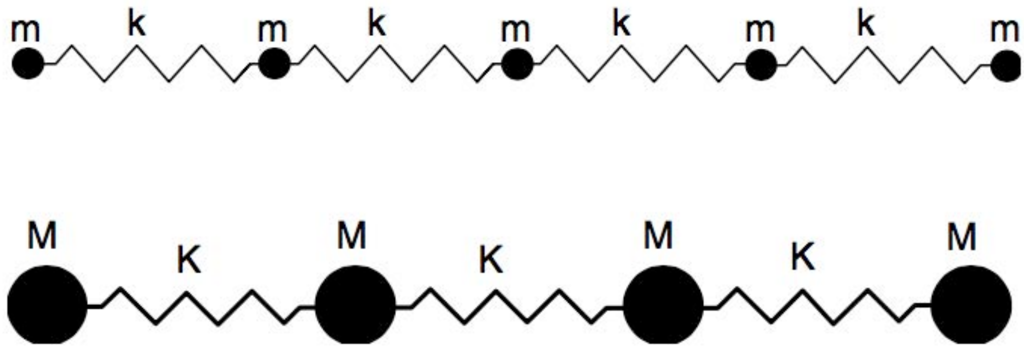

Figure 1.9 Conceptual diagram of acoustic impedance [5].

Table 1.1 Acoustic parameters for typical materials [16].

Material	Mass density kg/m^3	Compressibility $10^{-12} m^2/N$	Sound velocity m/s	Acoustic impedance MRayls
Biological materials				
Fat	950	508	1440	1.37
Neurons	1030	410	1540	1.59
Blood	1025	396	1570	1.61
Kidney	1040	396	1557	1.62
Liver	1060	375-394	1547-1585	1.64-1.68
Spleen	1060	380-389	1556-1575	1.65-1.67
Muscles	1070	353-393	1542-1626	1.65-1.74
Bone	1380-1810	25-100	2700-4100	3.75-7.4
Non-biological materials				
Air (0°C)	1.2	8×10^{-6}	330	0.0004
Rubber	950	438	1550	1.472
Fresh Water	988	452	1497	1.48
Salt Water	1025	416	1531	1.569
Polystyrene	1120	143	2500	2.8
Hard PVC	1350	175	2060	2.78
Typ. Araldit	1200	160	2300	2.8
Silicon, RTV-11	1260	739	1000	1.26
Quartz	2650	11.4	5750	15.2
PZT-5A	7750	5.65	4350	33.71
Gold	19290	4.93	3240	62.5
Aluminum	2875	9	6260	18

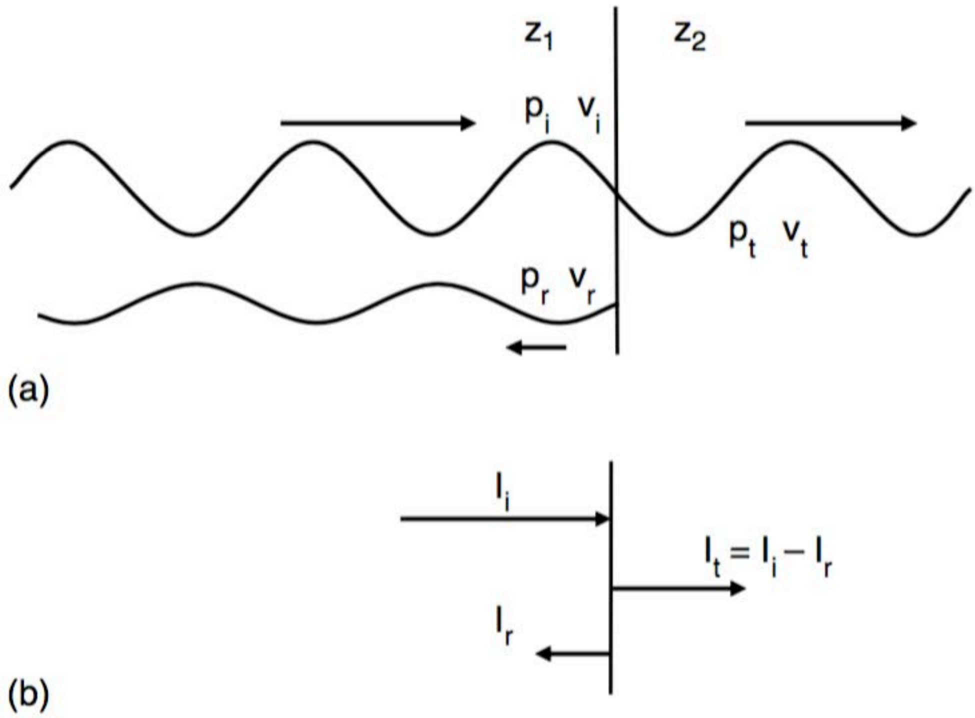

Figure 1.10 Acoustic wave travelling through two mediums [5].
(a) A waveform is travelling through two mediums. (b) The intensity of the waves in two mediums including the incident wave (i), reflected wave (r) and transmitted wave (t).

When the acoustic wave propagates from the active layer through the medium with different acoustic impedances, part of the acoustic wave is reflected by the interface and the rest passes through the interface and transmitted to the medium (shown in Figure 1.10) [5]. The wave reflection ratio depends on the difference of acoustic impedances between the active layer and the medium. A reflection coefficient represents the amplitude (R_A) and intensity (R_i) of the reflected wave compared with those of the incident wave. The amplitude and intensity coefficient are given by [5]:

$$\frac{I_r}{I_i} = R_i = R_A^2 = \left(\frac{Z_2 - Z_1}{Z_2 + Z_1}\right)^2 \quad (6)$$

The total intensity of the reflected wave and transmitted wave must be equal to the intensity of the incident wave, so the intensity transmission coefficient is:

$$T_i = 1 - R_i = (4Z_1Z_2)/(Z_1 + Z_2)^2 \tag{7}$$

Form Eq.(7), the intensity of reflected wave reduces with smaller acoustic impedance difference between two mediums. To reach the maximum intensity of transmission wave, the difference between the active layer and the loading medium should be reduced as low as possible. A matching layer is one of the solutions. Since most of the piezoelectric materials have significantly high acoustic impedance (≥ 20 MRayls) than the biological target being interrogated (front loading), such as human tissue ($1.5 - 3$ MRayls) and organs, an acoustic impedance gradient layer between the active layer and the front loading medium would help enhancing the transmission intensity by adding a matching layer between them.

To optimize the transmission intensity, the matching layer should match the acoustic impedance of the material chosen for each layer. Some combinations of the acoustic impedance used in each layer are listed in Table 1.2 [17], [18].

Table 1.2 Impedances of matching layer in different schemes [17], [18].

	Z_1	Z_2	Z_3
Single matching layer	$Z_p^{\frac{2}{3}} Z_r^{\frac{1}{3}}$		
Double matching layer	$Z_p^{\frac{4}{7}} Z_r^{\frac{3}{7}}$	$Z_p^{\frac{1}{7}} Z_r^{\frac{6}{7}}$	
Triple matching layer	$Z_p^{\frac{11}{15}} Z_r^{\frac{4}{15}}$	$Z_p^{\frac{1}{3}} Z_r^{\frac{2}{3}}$	$Z_p^{\frac{1}{15}} Z_r^{\frac{14}{15}}$

In Table 1.2, Z_r is the acoustic impedance of the front loading (Z_r of water and biomedical tissues $\approx$ 1.5 MRayls) and Z_p is the acoustic impedance of the active layer. It should be noted that Z_1 is the acoustic impedance of a matching layer casted directly on the active layer while Z_3 is the acoustic impedance of a matching layer contacted to the loading medium. The double matching layer for optimizing the transmission intensity is commonly used in ultrasound transducers produced by Philips, Vermon, etc. For reaching the maximum transmission of the acoustic wave to the loading medium, the design is to optimize not only the impedance of the matching layer, but also the thickness of each matching layer. Ideally, the exact one-quarter-thick matching layer would allow a 100% transmission of wave to the medium due to the total destructive interference of wave reflected by the matching. According to the energy equilibrium, full transmission is achieved due to zero energy reflected by the matching. Figure 1.11

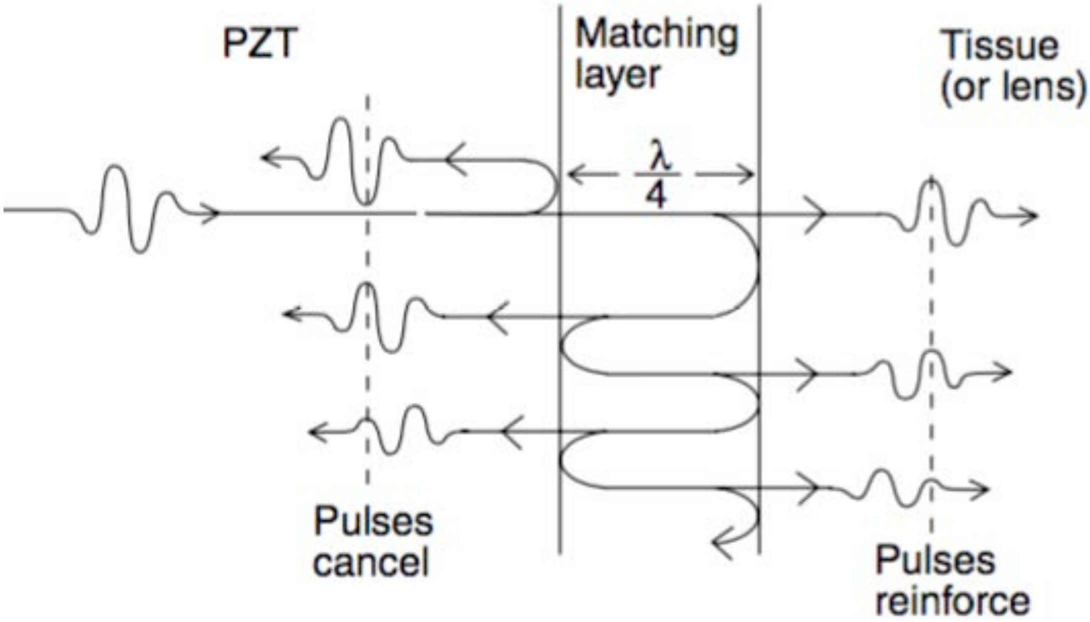

Figure 1.11 Quarter-wavelength matching layer interference [5].

illustrates the mechanism of quarter-wavelength matching layer [5]. The thickness of the matching layer would affect the center frequency of the pulse due to more energy at that frequency obtained from the loading medium. The ultrasound pulse with the frequencies closed to the center frequency can also achieve high-energy transmission. By enhancing the transmission of adjacent center frequency, the bandwidth of the transducer can be further widened. Thus, the frequency of matching layer with the best transmission is different from the center frequency of active layer, and the matching layer with ideal quarter-wave length thickness may not exhibit the widest bandwidth. Therefore, simulation is required to perform to estimate the thickness of matching layer for maximizing the bandwidth. The method to estimate the maximum bandwidth will be described in Chapter 2.1.

In conclusion, the matching layer is an important component for optimizing the performance of the ultrasound transducer. It can enhance both the sensitivity and the bandwidth of the ultrasound transducer.

1.2.3.4 Backing layer

The vibration of the active layer affects the particles on its both sides. A huge acoustic impedance difference at the backward propagation direction causes a high reflection. Figure 1.12 shows the pulse-echo waveform in both time and frequency domains investigated by Persson *et al.* 1985 [19]. All the results were obtained by the transducers without the matching layer. The transducer without a backing layer had a strong continuous fluctuation (ring-down) in the time domain while the bandwidth in the frequency spectrum is narrow with many peaks. With a backing layer, the ring-down of transducer was significantly shortened and the vibration in the frequency domain was abridged, moreover, the widest bandwidth was obtained from the transducer with the backing layer with the highest acoustic impedance. The comparisons show that the acoustic wave reflected back to the active layer influences the echo signal. The superposition of pulse length becomes longer, reducing the bandwidth and the axial resolution of the ultrasound transducer. The main function of the backing layer is to absorb the energy of the backward propagated acoustic wave as much as possible to prevent the wave reflected back to the active layer. For the backing layer with higher acoustic impedance, the smaller impedance difference between the active and backing layers would allow more acoustic energy transmit and being absorbed in the backing layer. If the impedance of backing layer is low, a large amount of energy will be reflected by the interface between the active layer and the backing layer, causing a stronger and longer ring-down. However, too much energy absorption would also cause lower sensitivity of transducer. This phenomenon is indicated in Figure 1.12 [19]. The echo amplitude became smaller with using the high-impedance backing layer.

To perfectly absorb the reflected acoustic wave, the backing layer should have a high acoustic attenuation. Attenuation is divided into three main parts that are absorption, reflection and scattering. Absorption is simply to convert the energy into heat. When the wavelength is much smaller than the object size, reflection dominates. On the other hand, scattering occurs when the wavelength is either comparable or greater than the dimensions of the object.

Absorption is caused by the viscosity and relaxation phenomenon of the medium. The equation of the absorption coefficient related to the frequency is expressed by the following equation:

$$\alpha = 2\omega^2\eta / 2\rho c \tag{7}$$

where $\eta = \mu / j\omega$, μ is the Lame constant and also called the shear modulus, ρ is the density and c is the velocity. From Eq. (7), the absorption of the backing layer is higher if the center frequency (ω) of the transducer increases. Relaxation is dependent on the relaxation time of the particle in the medium that is defined as the time that the particle needs to return to its original position after the acoustic wave propagation. The energy lost in the relaxation is smaller if the relaxation time is shorter than the wavelength. If the relaxation time is longer than the period of the wave, the particle cannot return to its original position before the next period. The acoustic energy will be lost to overcome the returning energy of the particle. However, if the frequency is high enough such that the particle cannot respond with the wave motion, the energy lost caused by the relaxation can be ignored. The relaxation is described using the following equation:

$$\alpha_r = \frac{B \cdot f^2}{1 + (f / f_R)^2} \tag{8}$$

where α_r is the absorption coefficient, f_R is the relaxation frequency, and B is a constant.

Scattering is similar to the reflection but with a relatively small scale. It happens with the medium with a small surface area, such as particles. For a particle with a size much smaller than the wavelength, scattering occurs in all directions uniformly. On the other hand, if the particle has a size comparable with the wavelength, the scattering direction is only in a wide angle.

After optimized the above factors, the attenuation of the backing layer can be

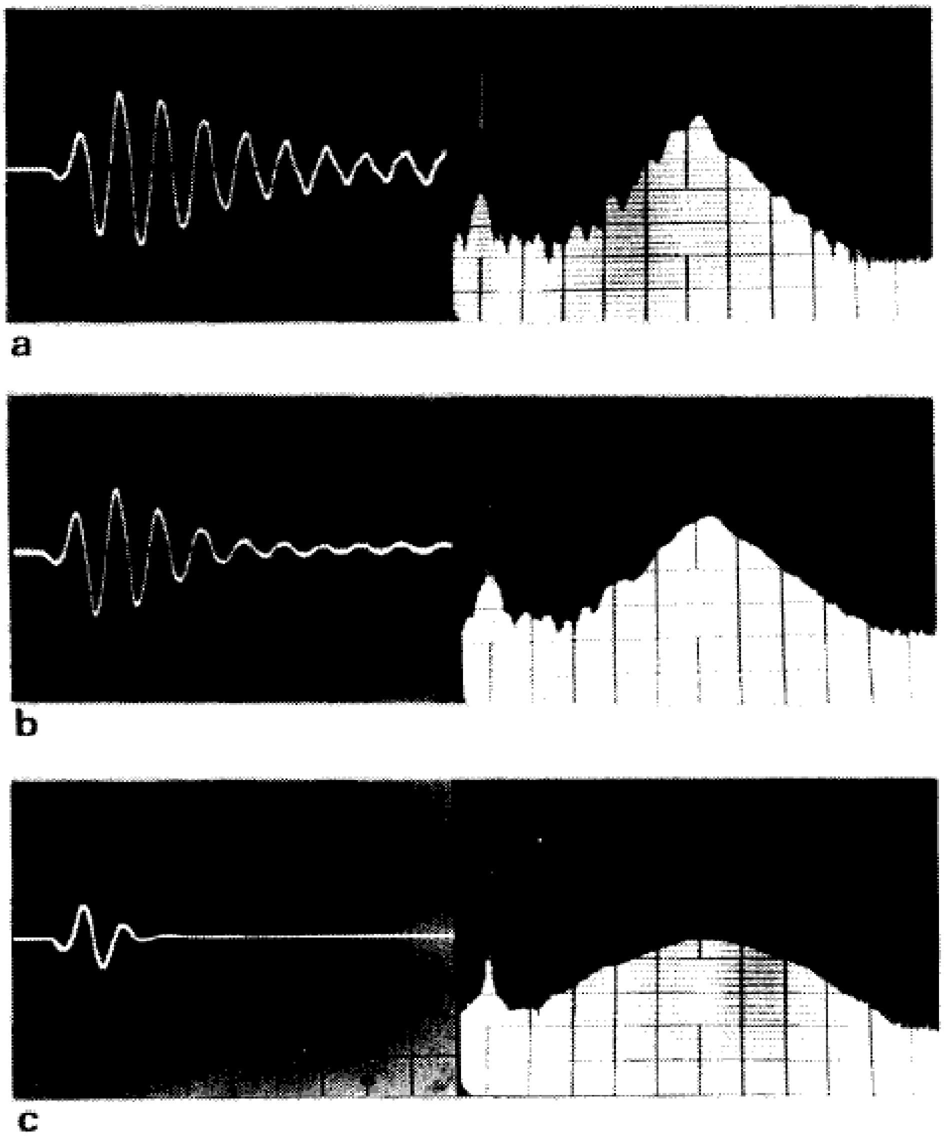

Figure 1.12 Pulse-echo and frequency spectra obtained in an experimental echo system [19]. All transducers have a backing layer only with (a) an air backing, Z_B = 0 MRayls; (b) a light backing, Z_B = 5 MRayls; and (c) a heavy backing, Z_B = 24 MRayls.

maximized to absorb the backside reflected acoustic wave, achieving a wide bandwidth. Unfortunately, the transducer with a higher attenuated backing layer possesses lower sensitivity. The compromising between the bandwidth and the sensitivity is the critical consideration in the backing layer design.

1.3 CONCLUSION

In conclusion, this chapter has explored the motivation and working mechanism of ultrasound transducer for medical imaging. When comparing with other diagnostic tools, the ultrasound transducer is with highly potential. The features of non-invasiveness and portability are the most prominent merits of the ultrasound transducer. However, the relatively low resolution and penetration of ultrasound transducer are needed to enhance to achieve high imaging quality of other diagnostic tools. According to this, optimizing the resolution and maintaining reasonable sensitivity makes the ultrasound transducer become the best diagnostic tool. For the working mechanism and theory, the ultrasound transducer is a device that transfers the electrical energy to the acoustic energy, and vice versa. By understanding the working mechanism of each part of ultrasound transducer, the ultrasound transducer can be further improved depending on various requirements.

In the following chapter, literature review will be explored for finding the research gap of this study, simultaneously, compensating the disadvantages of ultrasound transducer.

CHAPTER 2 LITERATURE REVIEW

2.1 MATERIAL SELECTION OF ACTIVE LAYER

In this chapter, different studies on transducers and materials are compared to determine the research gap and the materials used in this study.

Ultrasound transducers with high imaging resolution are essential for clinical applications, such as dermatology, intravascular imaging and ophthalmology, so the research effort has been spent on developing high-frequency transducers. Several studies have been reported to investigate ultrasound transducers with a frequency higher than 20 MHz [20]-[24] [31]. However, only few investigations have developed the transducers with high -6 dB bandwidth (higher than 70%) and high sensitivity (insertion loss ≤ 30 dB) [20], [25]. Although the lateral resolutions of those transducers were enhanced by the increment of frequency, the axial resolution was still a critical problem due to the relatively narrow bandwidth. As the axial resolution is directly related to the piezoelectric properties, the improvement can be achieved by enhancing the piezoelectric properties of active layer or replacing the material with better piezoelectric properties.

Lead zirconate titanate (PZT) ceramic is a piezoelectric polycrystalline material that has

Table 2.1 Properties comparison of PMN-PT and PZT materials [26].

Properties	PZT-5A	PZT-5H	PMN-0.3PT Single Crystal
Density, ρ ($\times 10^3 kg/m^3$)	7750	7500	8000
Dielectric constant before poling, ε_r, at 1 kHz	1600	2800	6000-7000
Dielectric constant after poling, ε_r, at 1 kHz	2000	3400	5000-6000
Dielectric loss, $\tan\theta$, at 1 kHz	2	2	< 0.1
Curie temperature (℃)	365	190	150
Electromechanical coupling coefficient, k_{33}	0.71	0.75	0.93
Height extensional vibration mode electromechanical coupling coefficient, $k_{33}^{'}$	0.68	0.68	0.82
Thickness extension mode electromechanical coupling coefficient, k_t	0.49	0.51	0.64
Piezoelectric charge constant, d_{33} (pC/N)	374	593	2500
Piezoelectric voltage coefficient, g_{33} ($\times 10^{-3} Vm/N$)	25	20	43
Acoustic velocity, v (ms^{-1})	4350	4560	3600
Acoustic impedance, Z ($\times 10^6 kg/m^2 s$)	34	34	29
Frequency constant, N_t ($Hz \cdot m$)	1890	2000	1800-1900

been widely used in ultrasound imaging application for commercial and research developments

for 40 years. The piezoelectric properties, such as piezoelectric charge coefficients and electromechanical coupling coefficients, of PZT are generally better than those of lead-free piezoelectric materials. The electromechanical coupling coefficient is a factor that illustrates the efficiency of energy conversion from the electrical energy to the mechanical energy, which is an extremely important factor for determining the -6 dB bandwidth, sensitivity, and even axial resolution of the transducer. Besides, the high-quality PZT with homogeneous performance can be fabricated by the proficient ceramic fabrication techniques. Those are the main reasons why PZT is popular as the active element of commercial ultrasound transducers. However, the performance of PZT is not the best even it has been significantly improved in recent decades. The high-end PZT only shows an electromechanical coupling efficiency of 70%, which is bounded by its imperfect dipole alignment. For achieving higher axial resolution of ultrasound transducers for biomedical imaging, a material with further better piezoelectric properties would be one of the promising solutions.

Piezoelectric single crystal materials, such as lead magnesium niobate doped with lead titanate, $Pb(Mg_{1/3}Nb_{2/3})O_3$-$xPbTiO_3$ (PMN-PT), and lead zinc niobate doped with lead titanate, $Pb(Zn_{1/3}Nb_{2/3})O_3$-$xPbTiO_3$ (PZN-PT), along [001] direction, have been reported to exhibit remarkable large electromechanical coupling coefficient and piezoelectric constant (k_{33} of 92% and d_{33} of 1500 pC/N) [27]. This opens up the possibility of making better-performance ultrasound transducers instead of using the

PZT ceramics as the active element. Table 2.1 illustrates the comparison of piezoelectric properties of PZT ceramics and PMN-0.3PT single crystal [26]. The main reason for their differences has been described in Chapter 1.2.3.1. Many previous investigations on low-frequency ultrasound transducers reported that the bandwidth could be improved by replacing the active material with better piezoelectric properties. Li *et al.* has compared two low-frequency (3.2 MHz) phased-array transducers using PZT ceramics and PMN-0.3PT single crystal, respectively, and found that the PMN-0.3PT single crystal transducer exhibited a -6 dB bandwidth of 76%, which was wider than the PZT ultrasound transducer [28]. PMN-PT single crystal does not only show its potential on the array transducers, but also the single-element transducers fabricated using the single crystal and its composites. Lam *et al.* has reported a 5-MHz PMN-PT single-element focused ultrasound transducer with a -6dB bandwidth of 70% and an insertion loss of 18.1 dB in 2011, which is within the wide bandwidth range [29]. The research of Oakley and Zipparo at 2000 [30] also reported that a PMN-0.32PT single crystal composite single-element transducer demonstrated a maximum bandwidth of 114%, which is a great enhancement compared to the PZT composite transducer.

The performance of reported ultrasound array transducers fabricated using PZT is shown in Table 2.2. In the table, all the ultrasound transducers are in a high frequency range from 20 MHz to 30 MHz. A 30-MHz linear-array fabricated using a PZT 2-2 composite investigated by Foster *et al.* 2009 has shown the highest -6 dB bandwidth, which is around 80%, and an insertion loss of 25 dB [31], [32]. The pitch of that linear-array was $\approx 1.5\lambda$, which was triple the theoretical value, but the bandwidth performance was out of the expectation. The wide bandwidth can still be obtained because the side beam has no adverse effect on the two-way pulse echo measurement. According to the descriptions, only one element was excited for emission and signal acquirement at the normal direction of the plane, thus the side beam was not received. However, the side beam effect may still occur during imaging. By comparing the two 20-MHz ultrasound transducers, the phased-array transducer fabricated by Chiu *et al.* [33] at 2014 has shown a bandwidth of 61% that is slightly wider than the linear array transducer investigated by Dinh *et al.* in 1996 [34]. The improvement may be attributed by the specifications of PZT material, but the piezoelectric parameters of the PZT were not all illustrated in both journals. This hypothesis is based on the fabrication technique improvement of PZT ceramic in recent decades. This may also be an evidence that the material with better piezoelectric properties can enhance the -6 dB bandwidth of the transducer. In summary, only one of the PZT transducers exhibited a bandwidth of wider than 70%, and 80% bandwidth was the widest in the high-frequency range array transducers. Jiang *el at.* has reported a 35-MHz PMN-PT 1-3 composite linear-array transducer for NDE applications in 2010. The transducer has shown a maximum bandwidth of 94% from one representative element, and its average bandwidth was around 75%. It shows that the PMN-PT array transducer has wider bandwidth than PZT one, moreover, its average bandwidth was also wider than most of the PZT array transducers. It may possible prove that the bandwidth of array transducer can be enhanced by replacing the active layer with PMN-0.3PT. If the hypothesis is right, by replacing the active layer with a material with better piezoelectric properties, the bandwidth of the developed phased-array transducer should have a wider -6 dB bandwidth compared to the previous research work.

Table 2.2 Specification and results of pervious investigated PZT ultrasound transducers

	Linear-array fabricated by Nguyen-Dinh *et al. 1996* [34]	**Phased-array fabricated by Chiu *et al.* 2014 [33]**	**Linear-array fabricated by Stuart Foster *et al.* [31], [32]**	**Linear-array fabricated by Jiang, *et al.* 2010 [35]**
Designed center frequency	20 MHz	20 MHz	30 MHz	35 MHz
Material	PZT-polymer composite	PZT-5H	PZT-polymer composite	PMN-PT 1-3 composite
Number of elements	128	48	256	64
Pitch	110 μm (~1.5 λ)	37μm (~0.5λ)	74 μm (~1.5λ)	132 μm (0.4λ in SiC)
-6 dB Bandwidth (Max)	50%	61%	N/A	94%
-6 dB Bandwidth (Average)	N/A	N/A	80%	75%
Insertion loss	46.4 dB	N/A	25 dB	>500mV (0 gain)

Although the ultrasound transducers fabricated using the PMN-PT single crystal exhibit outstanding performance compared to those fabricated using the PZT ceramics, the main drawback of the PMN-PT material is its low Curie temperature ($T_C \approx 130$℃) compared to the PZT ($T_C \approx 200$℃) [36], [37]. The Curie temperature represents a temperature that the material would lose the spontaneous polarization, which means its strain or vibration amplitude generated by the external electric field would remarkably degrade. This phenomenon would cause limitations on the fabrication process and applications. Re-poling may be required when the processing or operating temperature is higher than the Curie temperature. The performance of the re-poled ultrasound transducers may be lower. Nevertheless, biomedical imaging is usually performed with low power intensity at room temperature, so the thermal limitation for the applications can be neglected.

2.2 BEAM-FORMING METHOD

The transducers for ultrasound imaging can be classified into several typical types, such as single-element, linear sequential array, linear phased-array, etc. For the single-element ultrasound transducer, it has been fabricated to an ultra-high frequency range (up to 300 MHz) due to its relatively low complexity and simple fabrication process [38]. However, its imaging method relies on mechanical scanning in a line or arc pattern, so the imaging quality may be affected by the mechanical movement and the highest lateral resolution can only be achieved at the transducer focus. Moreover, the image processing is time consuming due to the slow scanning speed compared with the electronic scanning method. Besides, the friction induced by scanning the probe on the skin would cause discomfort on the patient in clinical ultrasound applications. Thus, the single-element ultrasound transducer is not an effective device for clinical imaging applications.

Other than the single-element transducer, a sequential linear-array transducer made of a large number of small active elements is an alternative. An insulator material is used to acoustically separate and physically connect the elements. The ultrasound beam produced by the elements is parallel to each other, and the beam propagation distance depends on the frequency. Comparing with the single-element ultrasound transducer, the scanning is faster because the electronic scanning technique with the higher imaging frame rate ($\geq$100 frames per second) [39] is employed. In the electronic scanning process, different groups of elements are excited by the electrical pulse, respectively, with specific time delays. The scanning area of linear-array is equal to its aperture size. If the target size is equal to the aperture size of linear-array, the linear-array can produce real-time images with a high frame rate. However, for a larger target, the number of elements needs to be increased, which would increase the fabrication complexity. Besides, with the divergence nature of acoustic wave, the near-field far-field distance is proportional to the area of the element group. The beam divergence happens beyond the near-field distance, and the lateral resolution and sensitivity are low in that region.

To improve the resolution and enlarge the scanning area, the sequential linear-array is set to be a phased-array. The only difference between the two arrays is that all the active elements of the phased array are electrically separated from adjacent elements. Each element is excited by an electrical pule in a certain time delay. The depth of focus and the beam angle can be tuned by exciting the elements in different time delays and phases during the scanning process as shown in Figure 2.1 [40]. By receiving the echo with the same manner of the single-element transducer, a real-time scan line is formed.

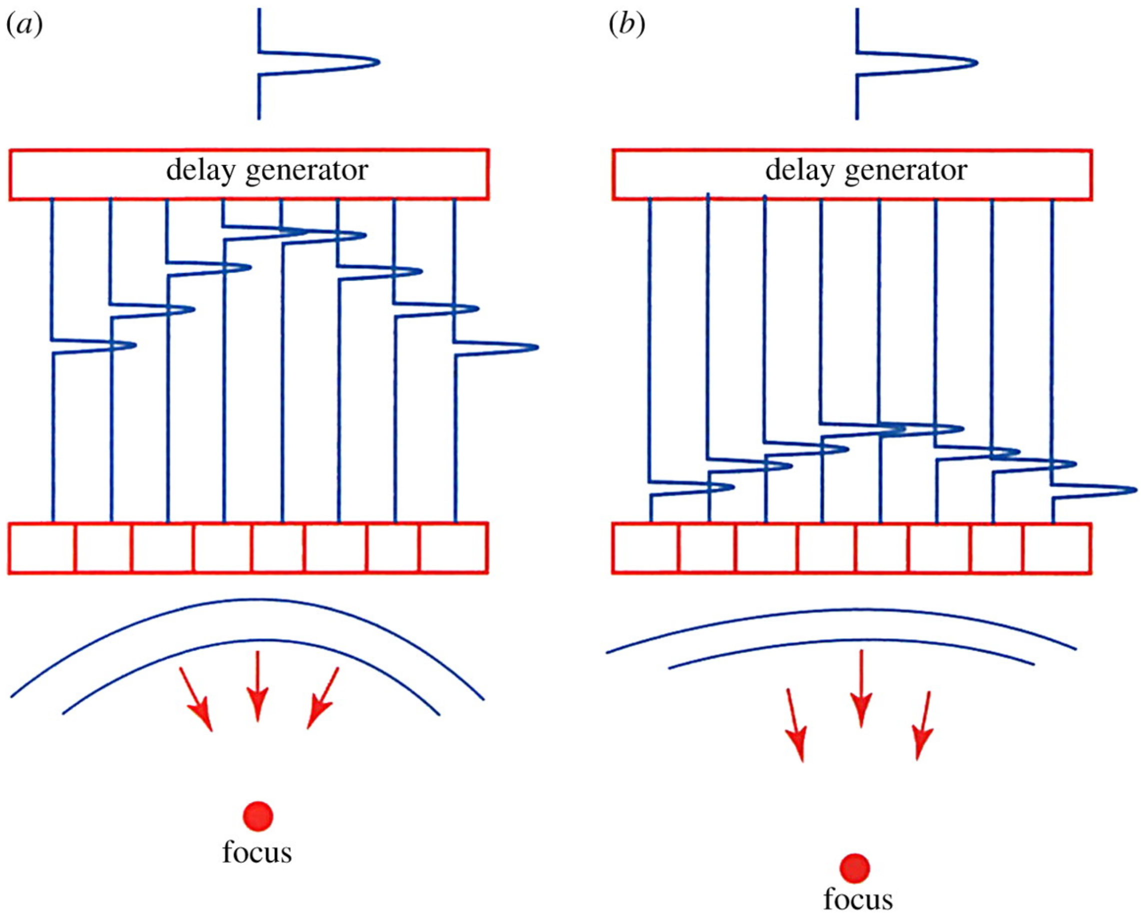

Figure 2.1 The focus profile of phased-array ultrasound transducer[40].
By exciting elements in a phased-array transducer with different time delays, the focal length of the beam can be adjusted.

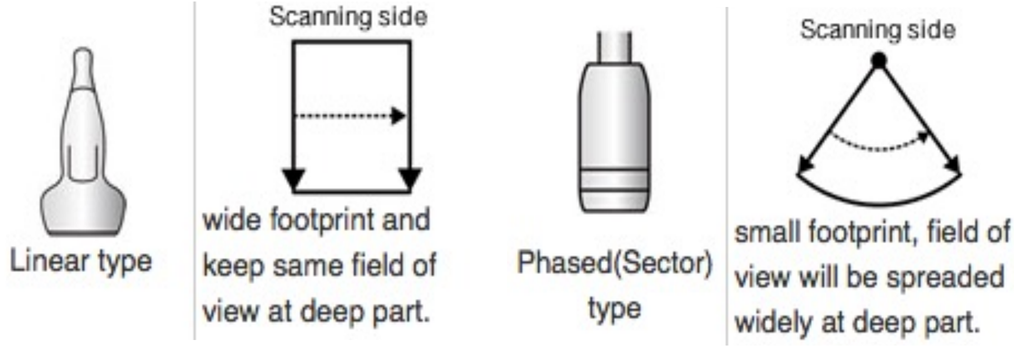

Figure 2.2 Fields of view of (a) a linear-array transducer and (b) a phased-array transducer [41].

By repeating the scanning with shifting the elements one by one, a real-time image is formed by the phased-array transducer. Because of having the steering angle, the phased-array transducer has a wider field of view in the far field compared to the linear-array. Figure 2.2 shows a field of view comparison between the linear-array and phased-array transducers [41]. In the far field, the field of view of the linear-array is nearly same as its aperture size without concerning the divergence of beam. The phased-array has a larger view of field that is proportional to the imaging depth due to the steering angle. Therefore, the linear-array is inappropriate for forward-looking intravascular ultrasound (FL-IVUS) and forward-looking endoscopic ultrasound imaging (FL-EUS) applications [42]. In short summary, the phased-array would have a dynamic focal zone with higher energy intensity for higher lateral resolution and sensitivity.

However, the phased-array has a critical requirement for distance separation between the elements that is called a pitch. The pitch of the elements is required to be $\lambda/2$ for diminishing the side beam interference of adjacent elements. The center frequency of the array is the main factor affecting the wavelength (λ). Figure 2.3 shows the relationship between the beam profile and the pitch value [26]. When a pitch is larger than $\lambda/2$, the side beam appears such that the main beam emitted by the side elements cannot be received. The relationship between the frequency and the wavelength can be found from the equation $v = f\lambda$, where v is the acoustic velocity in the travelling medium and f is the center frequency. Taking the water as an example of the travelling medium, the acoustic velocity in water is 1500 ms^{-1} and so the pitch of the array becomes extremely narrow when the center frequency is high. This would be the main difficulty for fabricating phased-array transducers with the center frequency of higher than 20 MHz. Previously, high-frequency phased array transducers ($\geq$20 MHz) fabricated with 1.0 ~ 1.2 λ pitch have been reported, for example, Beazanson *et al.* has reported a 40-MHz PMN-PT phased-array transducer with 1λ pitch at 2013 [43]. According to that study, the phased-array with 1λ pitch can still be appropriate for ultrasound imaging, but the $\lambda/2$ pitch is still the best theoretically.

To achieve the high lateral resolution with the narrow beam width, the phased-array transducer is the most appropriate selection. Moreover, the phased-array has a wider field of view due to the availability of the steering angle, which increases its generalization on biomedical imaging. However, the high electrical impedance and fabrication difficulty of phased-array are the main limitations, which may cause low sensitivity and unstable performance.

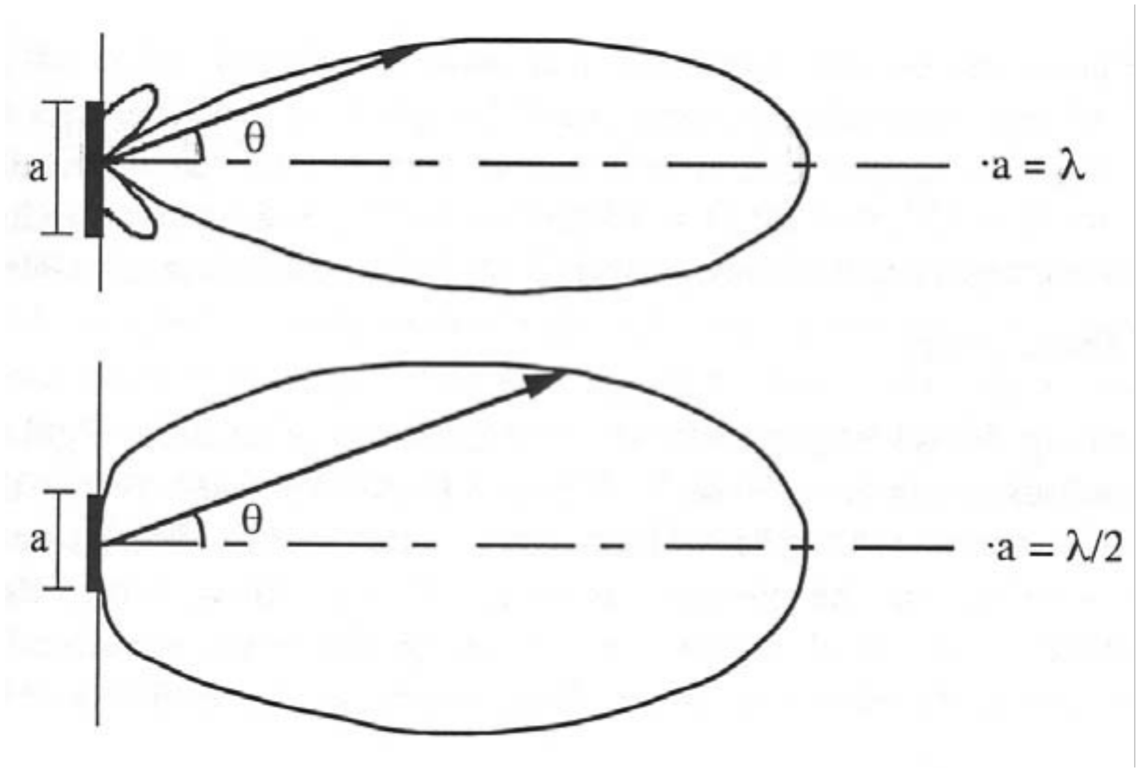

Figure 2.3 Beam profiles of transducer with different element widths [26].

2.3 ARRAY FABRICATION METHOD

Fabrication method is a key consideration that affects the performance and successful rate of the transducer. There are various methods to fabricate the arrays, such as “dice-and-fill” and chemical etching method [44]. The “dice-and-fill” method is the most common way to fabricate arrays using the bulk piezoelectric material [33], [42], [45], [46]. A mechanical dicing saw is used to dice kerfs with a designated width into the bulk piezoelectric material, and the kerfs will then be filled by the epoxy to enhance the electrical insulation between adjacent array elements. The filled epoxy can prevent the collapse of elements and reduces the crosstalk between the elements [47]. Some researchers have reported that filling the kerfs with a mixture of powders and epoxy can further reduce the crosstalk due to the shear wave propagated through the elements, translating to a higher resonant frequency when the volume fraction of the powder increases [9], [42]. However, the dice-and-fill method may not be an appropriate method particularly for fabricating ultra-high-frequency arrays when the blade width cannot fulfill the required kerf width between array elements.

Chemical etching and plasma etching are alternative techniques to fabricate the arrays. However, chemical etching is not unidirectional such that both depth and width are etched at the same time. Moreover, the final geometry after etched usually becomes trapezoid in the cross-sectional view. Thus, the chemical etching method is not suitable for the proposed high-frequency array design. On the other hand, the plasma etching is a better choice compared to the chemical etching. Plasma etching can be either isotropic that is same as the chemical etching or anisotropic to produce kerfs with the slower lateral undercut rate compared to its downward rate. Deep relative ions etching (DRIE), which is one of the plasma etching methods, can provide the optimized anisotropic etching profile with the depth to width etching ratio of higher than 30. Jiang *et al.* and Liu *et al.* have presented an PMN-PT 1-3 composite array transducer at 35 MHz [35] and an PZT array transducer at 50 MHz [48], respectively, fabricated by the DRIE method. Therefore, the DRIE method should be a suitable method for developing high-frequency array transducer with narrow kerfs.

Laser ablation is the other alternative promising method for high-frequency array development, which is a mechanical way using a high intensity laser to melt the piezoelectric material to form a precise kerf [31]. However, such high intensity laser is expensive, and the kerf profile may not be stable. Figure 2.4 shows the laser cutting array fabricated by Foster *et al* at 2009 [31]. The kerf-width was 8 μm, which is narrower than the physical limitation of mechanical dicing method, but the kerf-depth varied. It can be seen that some kerfs did not reach the backing layer, thus the crosstalk between those elements was higher. Besides, the heat generated by the laser may transform the material near the kerf from the crystalline phase into an amorphous phase, resulting in the degradation of the array performance.

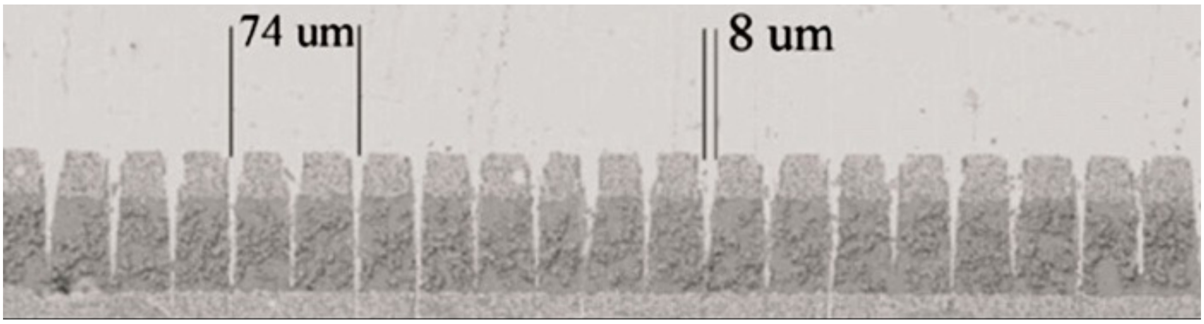

Figure 2.4 SEM of the elements using laser cuts [31].

2.4 OBJECTIVE

Based on the literature review, the PMN-PT single crystal material has shown the performance enhancement on ultrasound transducers. The PMN-PT single crystal is a promising material for developing wide-bandwidth ($\geq 80\%$) and high-frequency (20 MHz) transducers. The transducers fabricated using the PMN-PT single crystal are expected to implement high resolutions for small-scale biomedical imaging applications.

The beam forming method of phased-array ultrasound transducer is capable of achieving high lateral resolution and sensitivity for biomedical imaging without considering the influence of frequency. By using the PMN-PT single crystal with the outstanding piezoelectric performance and the dice-and-fill fabrication method, wide-bandwidth (~80%) 20-MHz phased-array transducers will be designed and developed in this project. In addition, the PMN-PT material with high dielectric constants is beneficial to the small-aperture transducers design. Thus, the proposed transducers have potential to be used in animals study for imaging small-scale tissues.

2.5 OUTLINE OF THESIS

Chapter 3 is the methodology. The procedure of using PiezoCAD, a simulation software assisting the transducer development, will be described. Meanwhile, the characterizations of piezoelectric materials, other acoustic layers and ultrasound transducers will be described, respectively.

Two designs and fabrication methods of 20-MHz PMN-PT single crystal phased-array ultrasound transducers have been investigated in this thesis. The details of designs and fabrication procedures will be illustrated in Chapter 4. Furthermore, the results and discussions of different designs will be presented in two subsections. At the end of Chapter 4, the results of the fabricated transducers will be compared with other reported high-frequency transducers.

Chapter 5 will be the conclusion of this thesis. The limitations and the drawbacks of the fabricated ultrasound transducer will be discussed. The improvement of the fabricated transducer will be elaborated in Future Work for further investigation.

CHAPTER 3 METHODOLOGY

In this Chapter, the modeling software for the transducer design will be presented. Furthermore, the characterization methods for piezoelectric and acoustic properties of materials and transducers will also be illustrated in detail.

3.1 MODELING OF ULTRASOUND TRANSDUCER

PiezoCAD (Sonic Concepts, Woodinville, WA) is an ultrasound transducer simulation programme based on KLM model of Krimholtz, Leedom and Matthaef [49], [50]. Figure 3.1 shows the KLM model's electrical component conceptual diagram of a transducer [47]. In the KLM model, the capacitor and inductor are employed to connect with certain formats to represent a ultrasound transducer with a piezoelectric element, matching layer and backing layer. Besides the KLM model, many different models, such as Mason model and Redwood model, can also represent the ultrasound transducer in an equivalent circuit mode and simulate its acoustic responses. The reason of choosing the KLM model in this project is its much physically intuitive compared to the other models.

In the PiezoCAD software, the properties of piezoelectric material, matching layer and backing layer can be input, and then the simulated results of pulse-echo response, frequency response and electrical impedance of the transducer can be predicted. Based on the requirements of the proposed research, the center frequency of the phased array transducer was 20 MHz and the acoustic impedance of the front loading medium was assumed to be 1.5 MRayls because the loading medium was water. Referring to Table 1.1, for the soft biomedical tissue, the acoustic impedance is around 1.5 MRayls to 2.0 MRayls. Thus, water was chosen as a medium for evaluating the performance of ultrasound transducer for medical imaging application. Actually, water can also be

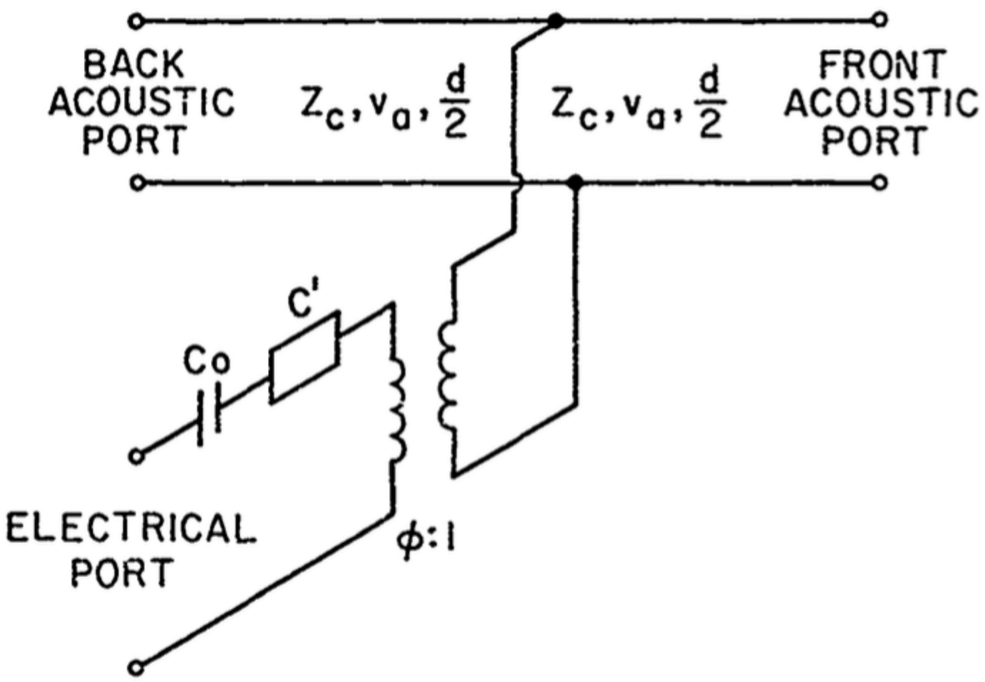

Figure 3.1 KLM model scheme [47].

selected for the back loading medium in some cases. Nevertheless, in this project, the acoustic impedance of backing layer was selected to be the back loading medium. The ideal backing layer should have an extremely high attenuation and relatively thick thickness to absorb nearly all the back-side reflection. In such case, no reflection is occurred from the back side, and so the thickness of the back side medium is considered to be infinity. After selected the frequency range and the loading conditions, the required parameters of all layers were input in the software. The measurement of piezoelectric parameters of material will be illustrated in Chapter 3.2.1 The required thickness of the piezoelectric material was theoretically calculated by $v/2 = f \cdot t$ in which the acoustic velocity measurement will be explored in Chapter 3.2.2.2, and experimentally measured by the thickness gauge (Model C112XB, Mitutoyo Corp., Japan). The thicknesses of the double matching layer were estimated using the quarter wavelength theory. The aperture size was set as the size of single active element based on the design. After input all the parameters, the PiezoCAD will display the two-way acoustic response and the electrical response of the designed transducer. By fine tuning the thickness of various layers and aperture size, the optimized result can be estimated.

3.2 CHARACTERIZATIONS

3.2.1 Piezoelectric properties

The piezoelectric properties of the piezoelectric material can be measured by using an impedance analyzer (4294A, Hewlett-Packard) and a piezoelectric constant meter. The impedance analyzer is an equipment that measures the electrical properties of the material or device. The working mechanism is simple. During the measurement, the equipment drives an electrical signal with a sweeping frequency on the material through an adapter and measures its electrical response. The sweeping frequency range is from 40 Hz to 110 MHz. To test the bulk material, an adapter 16034E (Hewlett-Packard) is used. A testing fixture 16047D (Hewlett-Packard) is used if the specimen is not a bulk material. Most piezoelectric properties can be measured by the impedance-theta (Z-θ) and parallel capacitance-dissipation factor (C_p-D) modes. The impedance and phase-angle responses with frequency of a typical piezoelectric bulk material are shown in Figure 3.2 [51]. For the impedance response, f_r and f_a are the resonance frequency and the anti-resonance frequency, respectively. Using the resonance frequency and the thickness, the frequency constant of the material can be calculated. The electromechanical coupling coefficient (k_t) can be calculated by the following equation:

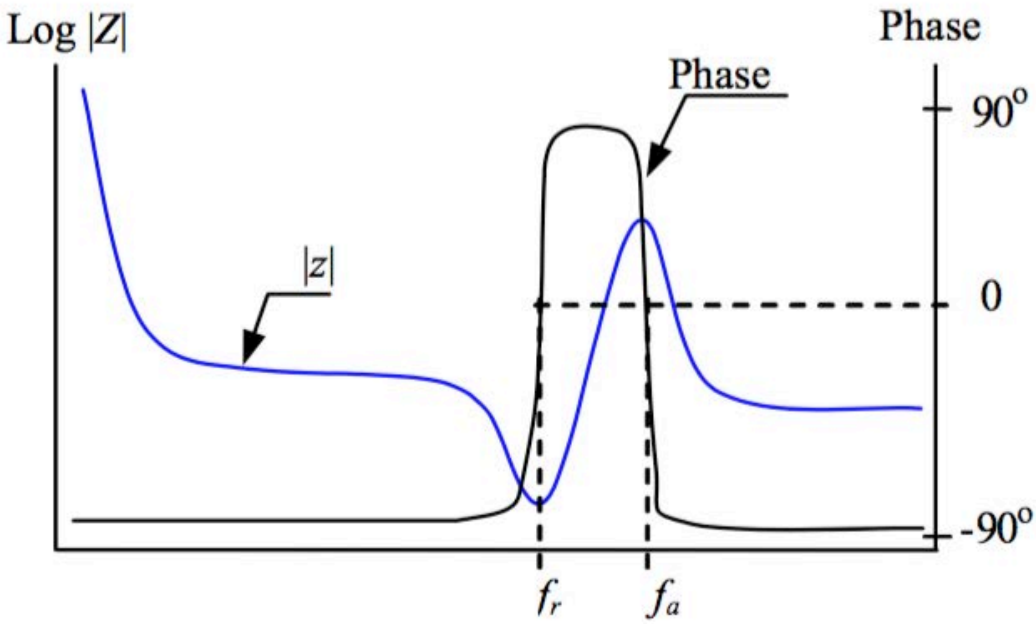

Figure 3.2 Impedance (blue line) and phase angle (black line) responses of a typical bulk piezoelectric material [51].

$$k_t^2 = \frac{\pi}{2}\cdot\frac{f_r}{f_a}\tan\left[\frac{\pi}{2}\cdot\frac{(f_a - f_r)}{f_a}\right] \tag{9}$$

Dielectric constant ε_r and clamped dielectric constant ε_c can be obtained at 1 kHz and $2f_r$, respectively, through the C_p-D measurement. The calculation is shown as follows:

$$C = \frac{\varepsilon_o \varepsilon_{r/c} A}{d} \tag{10}$$

where C is the capacitance at a certain frequency, A is the area of the electrode, d is the thickness and ε_o is the permittivity at vacuum ($= 8.854\times10^{-12}$).

The piezoelectric constant of the material was obtained by using the piezoelectric constant meter. The conceptual diagram of the working mechanism is shown in Figure

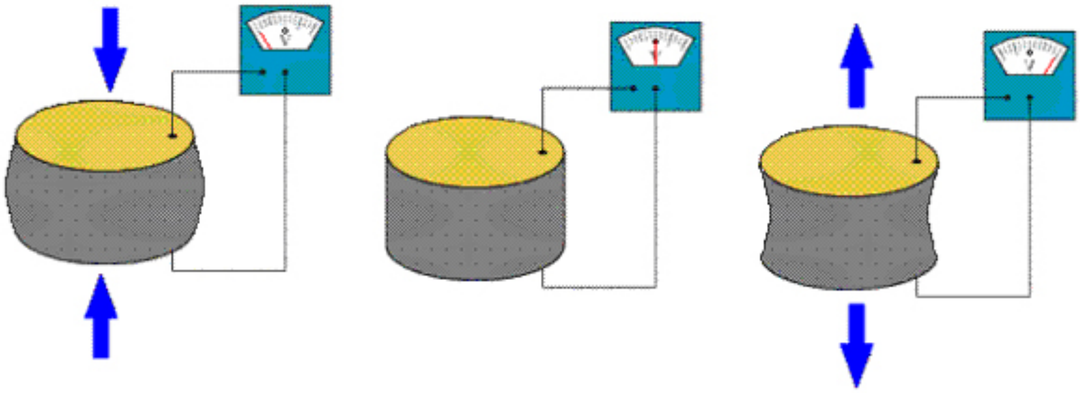

Figure 3.3 Working mechanism of piezo-meter [52].

3.3 [52]. The specimen is clamped by the driving probe that compresses the specimen with a fixed frequency. By measuring the generated voltage during the vibration, the piezoelectric constant is calculated and displayed.

3.2.2 Acoustic impedance

3.2.2.1 Density

The acoustic impedance measurement can be divided into two parts: density measurement and acoustic velocity measurement. Firstly, the density measurement was done by the Archimedes' principle. The weights of the specimen in air and immersed in water were measured by an electrical balance, respectively. With using the following equation, the density of the specimen can be determined.

$$\rho_{specimen} = \rho_{water} \cdot \frac{m_{air}}{m_{water}} \tag{11}$$

where ρ_{water} is the density of water (≈ 1000 kg/m^3). This measurement is limited by the density of the specimen that should be higher than that of water, and the specimen that should not exhibit strong water absorption effect. For the specimen not fulfilling the requirements, the fluid should be changed and the density of water should be replaced by the density of that fluid in Eq. (11).

3.2.2.2 Acoustic velocity

The acoustic velocity measurement setup is shown in Figure 3.4. The specimen clamped by an angle tunable fixture was placed between two identical ~10 MHz ultrasound transducers. The fixture can only rotate along the vertical direction for adjusting the angle between the propagation direction of the acoustic pulse and the normal of specimen along the thickness direction. One of the transducers was connected by a pulser/receiver (Panametrics 5900PR, Olympus) or a function generator (Tektronix AFG 3251) for acoustic pulse excitation. Another transducer was connected to a digital oscilloscope (HP Infinium) for receiving the propagated acoustic pulse. An acoustic coupling gel was filled in the gap between the specimen and transducer on both surfaces for enhancing the signal. The measurement has two main steps. First, the propagation time (t_o) of acoustic pulse without the specimen was measured by connecting both transducers head by head. The time was simply displayed on the oscilloscope. Second, the propagation time (t_s) with the specimen was measured. The connection between each surface should be as close as possible. Finally, the longitudinal acoustic velocity can be calculated by the following equation:

$$v_{33} = d / (t_s - t_o) \tag{12}$$

where d is the thickness of the specimen and v_{33} is the longitudinal velocity.

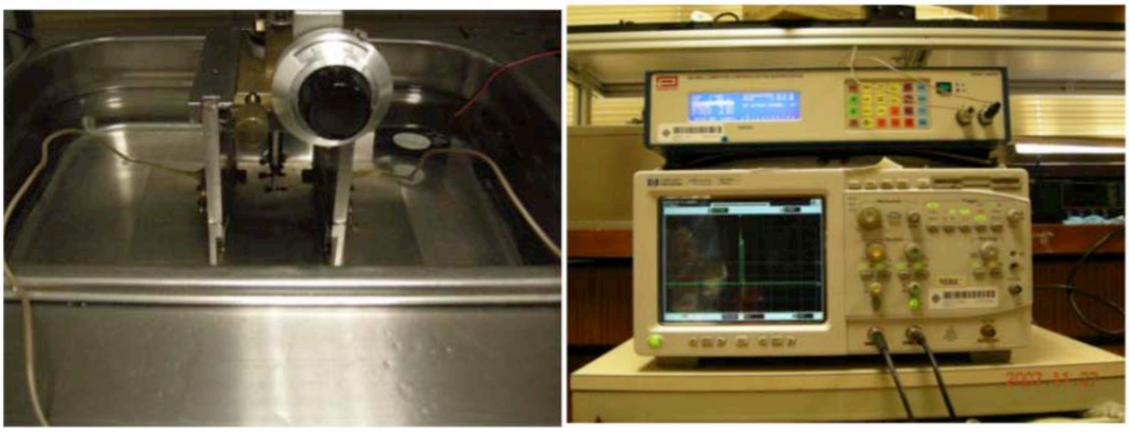

Figure 3.4 Setup for the longitudinal acoustic velocity measurement.

For the shear velocity measurement, a shear acoustic transducer was used. The measurement method is similar to the previous one. The pulse/receiver or the signal generator excites the shear wave transducer such that a shear acoustic pulse was propagated along the normal direction of the transducer. The specimen was clamped between the transducer and a 5-mm thick quartz. The propagated pulse and the pulse reflected by different interfaces were displayed by the oscilloscope connected with the transducer. The maximum amplitude of the reflected pulse was obtained by rotating the transducer along the normal direction. The time difference of two pulses reflected by different interfaces was measured by the oscilloscope. Using the following equation, the shear velocity of the specimen is calculated.

$$v_{shear} = 2d / t \tag{13}$$

where t is the time difference and d is the thickness of the specimen. Using the Eq. (5), the acoustic impedance of piezoelectric material, matching layer and backing layer were calculated.

3.2.3 Acoustic response of transducers

3.2.3.1 Pulse echo response and frequency spectrum

The pulse-echo response of the phased-array transducer was measured in a water tank at room temperature using a Panametrics 5900PR pulser/receiver. The echo was reflected by a thick (~37 mm) stainless steel target at a distance of the near field-far field (nf-ff) transition point. The nf-ff distance of element was calculated using the following equation:

$$N = A / \pi\lambda \tag{14}$$

Where A is the aperture of the element, λ is the wavelength of the acoustic pulse in the medium. The active element was excited by an electrical impulse of 1 μJ at 500 Hz repetition with 50 Ω damping and 26 dB gain. The time domain echo response was displayed using an oscilloscope (HP Infinium). The frequency domain echo response was calculated by the built-in Fast Fourier Transformation (FFT) programme. Figure 3.5 shows the measurement setup. Two -6 dB points in the frequency spectrum were found at the 6 dB difference from the maximum amplitude. The equation of bandwidth calculation is shown as follows [8], [28], [53]:

$$\text{-6 dB bandwidth} = 2(f_H - f_L)/(f_H + f_L) \tag{15}$$

where f_H and f_L are the frequencies of the -6 dB points.

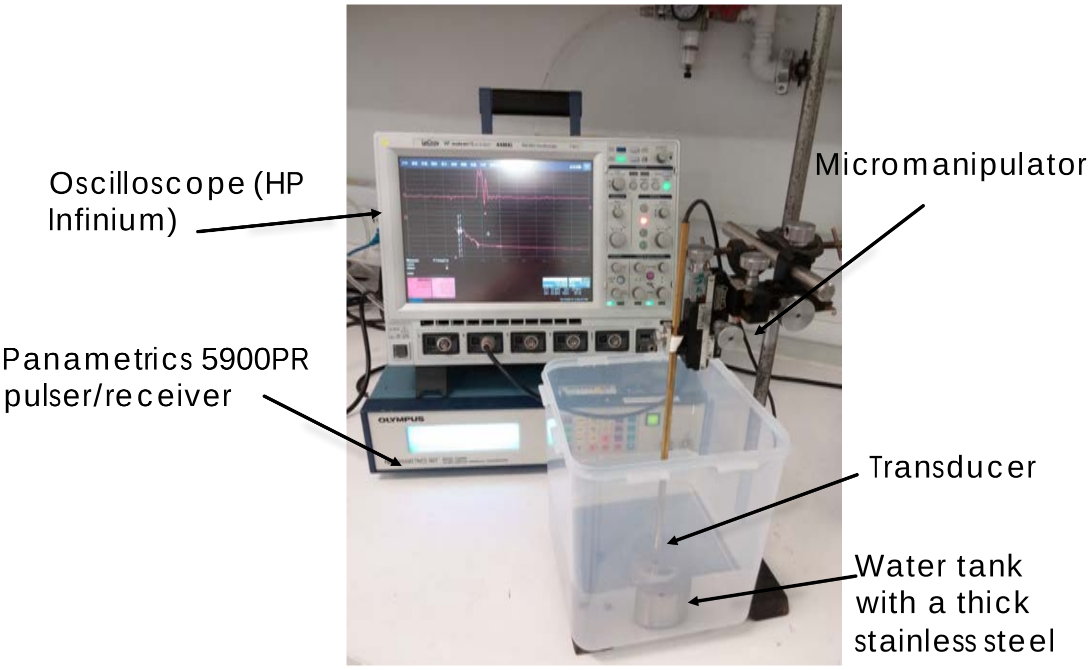

Figure 3.5 Setup of two-way pulse-echo response measurement.

3.2.3.2 Insertion loss

The insertion loss (*IL*) measurement setup is same as Figure 3.5. The transducer was excited by a signal generator. The excitation waveform was a 20-cycle sinusoidal wave with an amplitude V_i and a frequency of the center frequency in a tone burst mode. Actually, 5 cycles were enough to measure the *IL*. However, the measured results were much stable and accurate when the average value was taken in 20 cycles compared to 5 cycles. Thus, 20-cycle was chosen in the measurements [54]. The pulse propagated through the water and reflected by the interface between water and stainless steel. The amplitude (V_o) of the reflected pulse was obtained by the transducer and displayed on the oscilloscope connected with the signal generator and the transducer simultaneously. The impedance of the oscilloscope was set as $1\,M\Omega$ for V_o measurement and 50 Ω for V_i measurement. The following equation shows the calculation of *IL*:

$$IL = -20\log(\frac{V_o}{V_i}) \tag{16}$$

CHAPTER 4 RESULTS AND DISCUSSIONS

In this Chapter, three 20-MHz PMN-0.3PT single crystal phased-array transducers are going to present. The design of two arrays had slightly difference that Array 2 was the improved version of Array 1 resulting in higher performance and successful rate. The design, the detail of the fabrication procedure of different arrays and all the parameters will be illustrated in two sections. Simulated and measured results of the acoustic and electrical responses of those fabricated US transducers will be shown. Eventually, discussion and result comparison will be presented for elaborating the accomplishment of this study and the limitation of the fabricated ultrasound transducers.

4.1 ARRAY 1

4.1.1 Simulated result

The input parameters of the PMN-PT single crystal are shown in Table 4.1. The matching layer used in the first and second matching layers are $2-3$ μm aluminum oxide powder mixed with EPO-TEK 301-2 (Epoxy Technology Inc., Billerica, MA) (Epoxy 301) and pure Epoxy 301, respectively. By using Table 1.2, the calculated acoustic impedances of the double matching layer were 8.5 MRayls and 2.3 MRayls. The materials for the first and second matching layers had similar acoustic impedance and the non-conductive behavior. The non-conductive behavior was required because the separated electrodes were designed on the front surface for adhering to the custom designed flexible circuit (Hong Rui Kang Electron Co. Ltd, China). A conductive epoxy E-solder 3022 (Von Roll Isola, New Haven, USA) (E-solder) was used as the backing layer. E-solder had a high attenuation (112 dB/mm at 30 MHz) [55] in a wide frequency range, so it has been used as the backing layer in different research and commercial products [38], [56], [57]. The properties of the layers and the specifications of the arrays are listed in Table 4.2 and Table 4.3, respectively.

Table 4.1 Measured properties of the PMN-PT single crystal

Material	PMN-0.3PT
Longitudinal velocity (ms^{-1})	4200
Shear velocity (ms^{-1})	2100
Density (kgm^{-3})	7500
Dielectric constant, ε_{33}^{r}	~5000
Clamped dielectric constant, ε_{33}^{s}	1400
Piezoelectric constant, d_{33} (pC/N)	1400
Electromechanical coupling coefficient, k_t	0.60
Acoustic impedance (MRayls)	31.5
Loss tangent	0.005

Table 4.2 Array 1-Properties of acoustic layers

Matching layer number	1	2	Backing layer
Material	$2-3\mu m$ Al_2O_3 powder + ERO-TEX 301-2	EPO-TEK 301-2	E-solder 3022
Weight ratio	1.3:1	N/A	N/A
Acoustic impedance (MRayls)	7.6	3.0	5.9
Velocity (ms^{-1})	3320	2650	1850
Density (kgm^{-3})	2295	1132	3200

Table 4.3 Array 1-Specifications

Designed center frequency	20 MHz
Number of elements	64
Pitch	75 μm (1λ)
Elements width	55 μm
Elements length	5 mm
Elevation dimension	2.153 mm
Azimuthal dimension	4.8 mm
Kerf width	20 μm
PMN-PT thickness	80 μm
First matching layer thickness	40 μm
Second matching layer thickness	33 μm
Backing layer thickness	2 mm

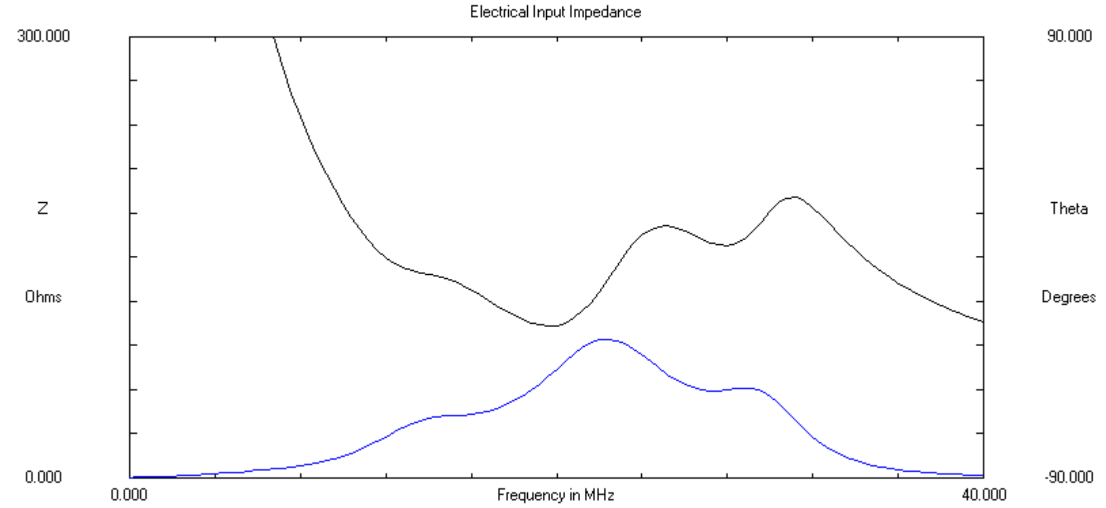

Figure 4.1 Array 1-Simulated electrical impedance spectrum.

The piezoelectric properties of the PMN-PT single crystal were characterized by the impedance analyzer. The sound velocity and density of acoustic layers in Array 1 were measured by using the sound velocity measurement setup and Archimedes drainage

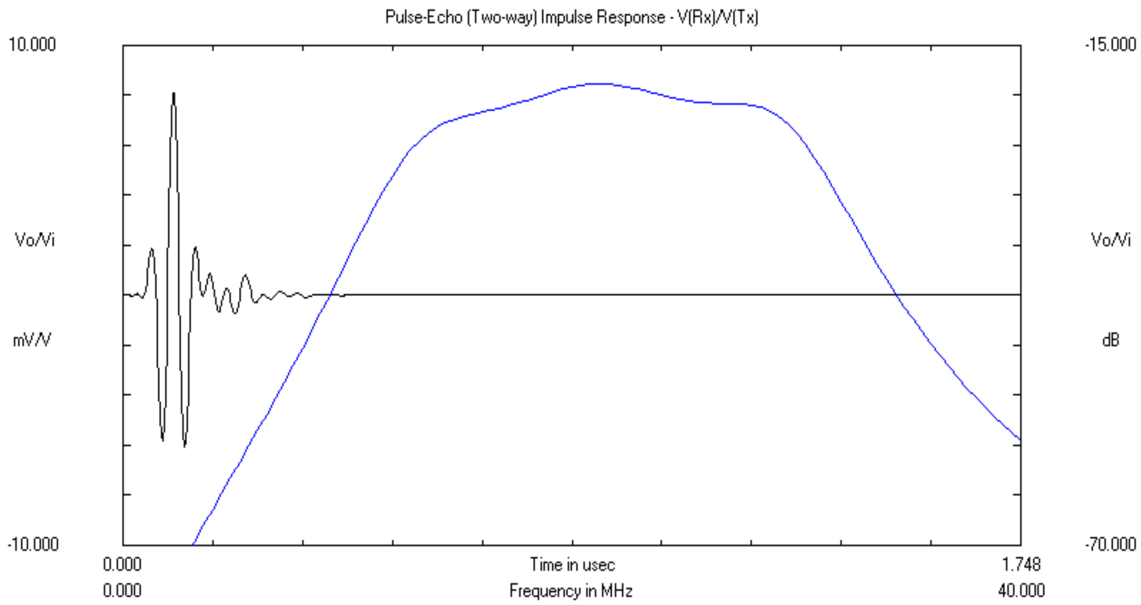

Figure 4.2 Array 1-Simulated pulse echo waveform and frequency spectrum.

method described in Chapter 3.2.2. The simulated results are shown in Figures 4.1 and 4.2.

Figures 4.1 and 4.2 show the electrical impedance responses and pulse-echo waveform modeled by PiezoCAD. The optimized thicknesses of the active layer and double matching layer were 80 μm, 40 μm and 33 μm, respectively. The E-solder with a thickness of 2 mm had high attenuation to absorb the reflected wave. In the pulse-echo waveform, the simulated center frequency was 21.7 MHz while the -6 dB bandwidth was 78%. The peak-to-peak value of simulated result was 11.3 mV/V. According to the results, the center frequency is slightly higher than the expectation, but it is still accepted. The thickness of PMN-PT was 80 μm that was thinner than the theoretical calculation (105 μm), causing the shift of the simulated center frequency. The center frequency of the array was compensated to maximize the bandwidth. Although the optimal simulated bandwidth is still slightly below 80%, this is still acceptable. The electrical impedance spectrum showed the impedance of 101 Ω @ 20 MHz that was double the requirement of 50 Ω due to the small aperture size. The aperture size could not be further increased due to the technical limitation of dicing saw. By increasing the width of element while remaining the pitch unchanged, reducing the kerf is the only compensation, but the kerf width has reached the physical limitation of the dicing blade.

Although the thinnest blade used to dice the PMN-PT single crystal was $15\,\mu m$, the dicing blade vibrates during the high speed rotation so that the resultant kerf should be wider. Thus, the width of element cannot be further increased. Increasing the element length may be the only option to increase the aperture size, but the electromechanical coupling performance may reduce because the resonance mode would change according to the dimensions of the element. The high impedance issue can be solved by using an electrical coupling system to match the high-impedance array to 50 Ω send/receive electronics [9]. In general, the reduction of electrical impedance of the transducer would enhance its sensitivity.

4.1.2 Fabrication procedures

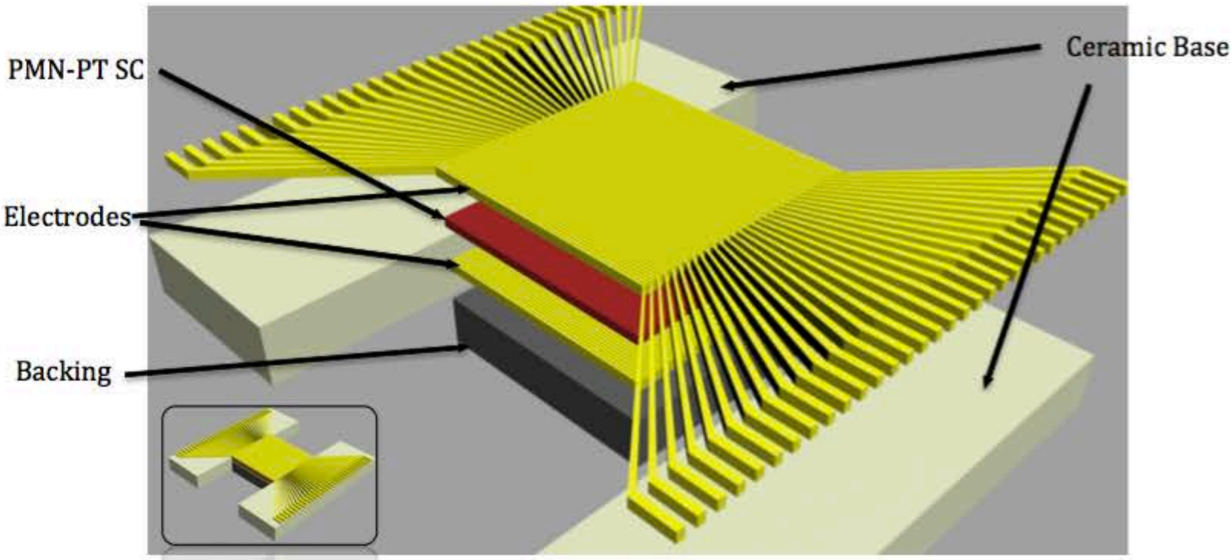

Figure 4.3 Schematic of Array 1.

The fabrication procedures of ultrasound transducer depend on its design. For Array 1, the schematic structure is shown in Figure 4.3. The fabrication method used was the “dice-and-fill” method. At first, the piezoelectric material was sputtered with chrome/gold (Cr/Au) electrode (thickness ~ $200nm/500nm$) on both surfaces using magnetron sputtering. Then, the sample was poled under a DC electric field with an amplitude of $1\ \mathrm{MV/m}$ in methyl hydrogen polysiloaxane (Silicon oil) at 120 ^{0}C for 15 mins. The voltage was kept until the poling temperature returned to the room temperature. The sample was then short-circuited for 24 hours to remove trapped charges that may cause self-depolarization.

After the poling process, the sample was diced into a dimension of $5mm\times5mm$ by a dicing saw (model DAD 321, DISCO, Japan) and lapped to a thickness of $0.13mm$ after casting the backing layer (E-solder) on the backside of the sample. The E-solder was centrifuged with 3000 rpm for 10 minutes for better adhesion. Then, the E-solder was cured in an oven set at room temperature for 24 hours. The array was then fabricated by using the dicing saw to dice the sample into 32 elements with a kerf of $27\ \mu m$ and dicing spacing of $150\ \mu\mathrm{m}$. The dicing depth was $150\ \mu\mathrm{m}$ with a cutting speed of $0.4\ \mathrm{mm/s}$, which should certainly be enough to dice through the $130\ \mu\mathrm{m}$-thick sample. The kerf was filled by epoxy 301 to reduce the crosstalk between the elements [47]. After filling the epoxy, the sample was degassed in vacuum to remove air bubbles inside the kerfs. The surface of the sample was polished to remove the epoxy covering the surface, then the total sample thickness became 110 μm. The sample was diced again with a spacing of 150 μm by aligning the middle of the elements as a reference point.

After dicing, the mentioned epoxy filling and polishing process were repeated again. After the dice-and-fill process, two ceramic plates were placed next to the sample as a base for the electrode extension. Since the ceramic is harder than the epoxy, it can

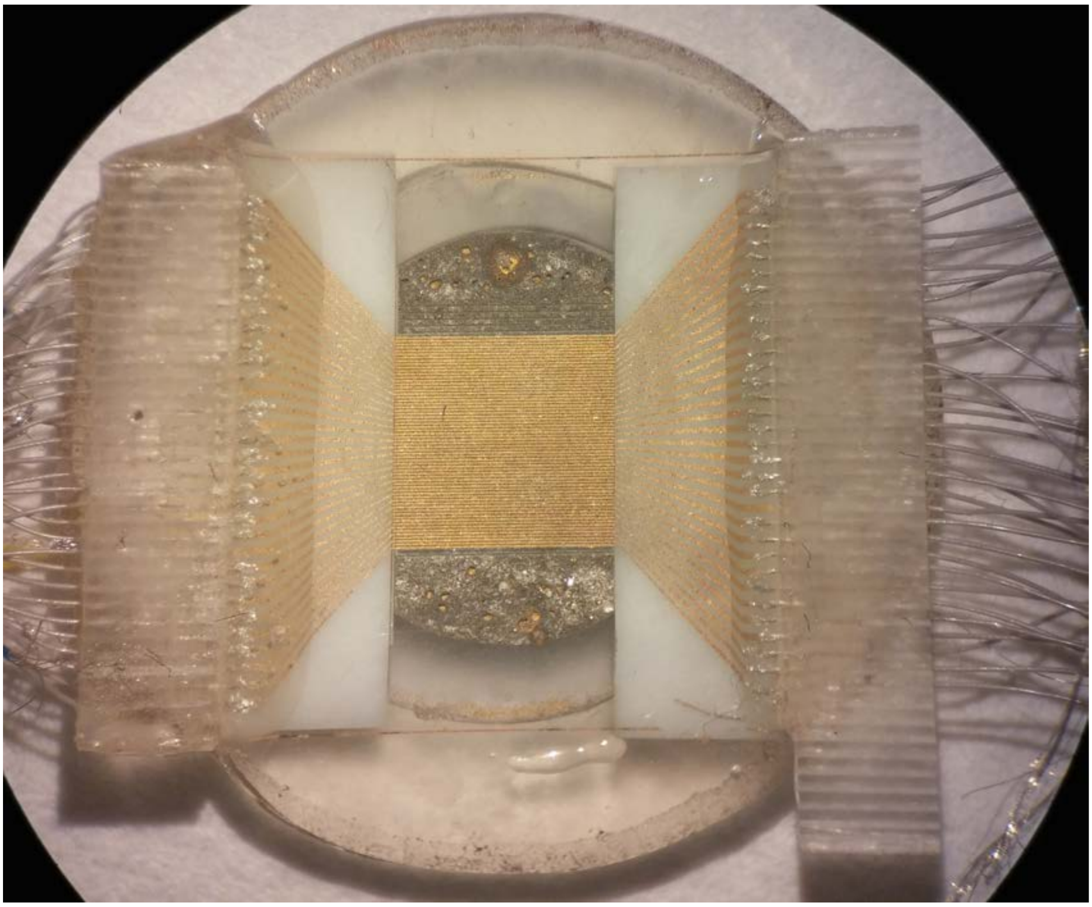

Figure 4.4 Array 1-Top view of the 64-elements array after wire connection.

provide a stable base for electrodes connecting with coaxial cables because the adhesion between Cr/Au electrodes and epoxy is weak that the electrodes may disconnect with the array afterwards. Then, the array was further lapped to the simulated thickness (80 μm) using alumina powder that can remove the scratches on the array surface to enhance Cr/Au electrodes adhesion. A 200 nm-thick Cr/Au electrode was sputtered on the sample surface and then etched into an electrode pattern by using photolithography (Aligner 800MBA). The Au and Cr electrodes were etched using potassium iodide (KI), and mixture of cerium(V) ammonium nitrate and nitric acid with the etching time of 30 s and 60 s for Au and Cr, respectively. The anode (end of the extension electrodes) was wired to the coaxial cable while the cathode was connected to the backing layer using a conductive epoxy, E-solder. The epoxy was finally covered on the connection nodes of the coaxial cables for protection. A 3 μm-thick Parylene C was coated on the whole array by the Parylene C deposition system (Specialty Coating System, Inc., USA) for preventing water invasion and chemical hazards. Figure 4.4 illustrates the appearance of Array 1 after the wire connection.

4.1.1 Characterizations

The electrical impedance of transducer was characterized by the impedance analyzer. Figure 4.5 shows the measured electrical impedance and phase angle of a representative element of Array 1 in the frequency domain. All the important parameters are listed in Table 4.4 and compared with the simulated results. Array 1 shows a phase angle peak at 19.4 MHz. The center frequency was slightly lower than the designed frequency, and the impedance was slightly higher. Both time domain and frequency domain echo responses of the representative element of Array 1 are shown in Figure 4.6 and the main properties are listed in Table 4.5. Array 1 showed a center frequency of 22 MHz that is close to the design. Since Array 1 was the first prototype to check the material and fabrication issues, no matching layer was employed, the bandwidth was low (41%) that is significantly lower than the simulated result (78%). The simulated results of acoustic responses are also listed in Table 4.5 for comparison.

Table 4.4 Array 1-Comparison of simulated and measured electrical properties

	Measured	Simulated
Impedance (Ω)	135 Ω @20 MHz	101 Ω @20 MHz
Resonance frequency, f_r (MHz)	16.3	19.0
Anti-resonance frequency, f_a(MHz)	21.4	19.7
Effective coupling coefficient, k_{eff}	0.43	0.69

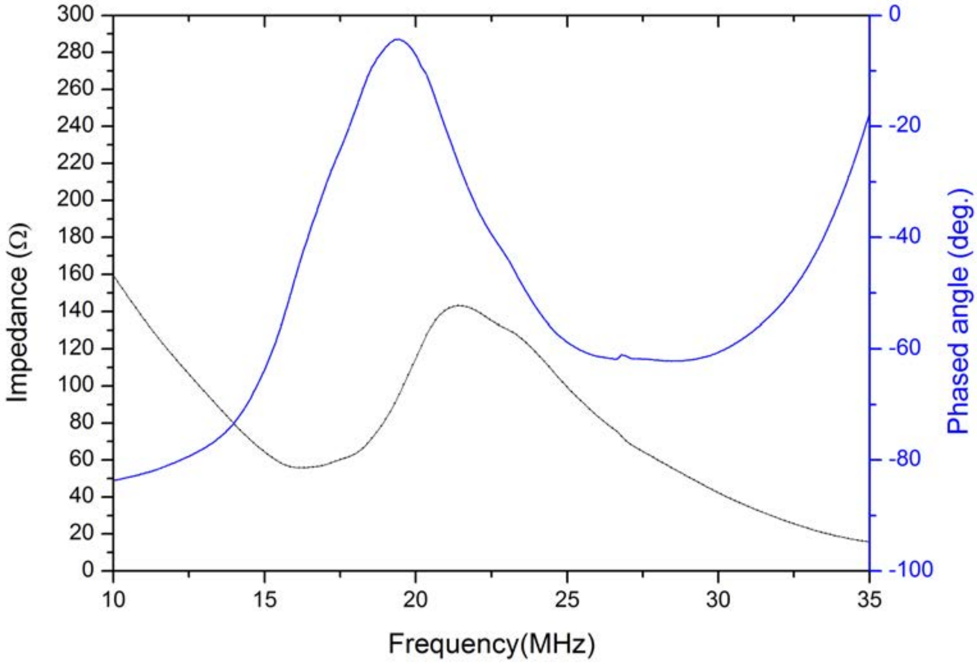

Figure 4.5 Array 1-Measured electrical impedance (black line) and phase angle (blue line) of a representative element.

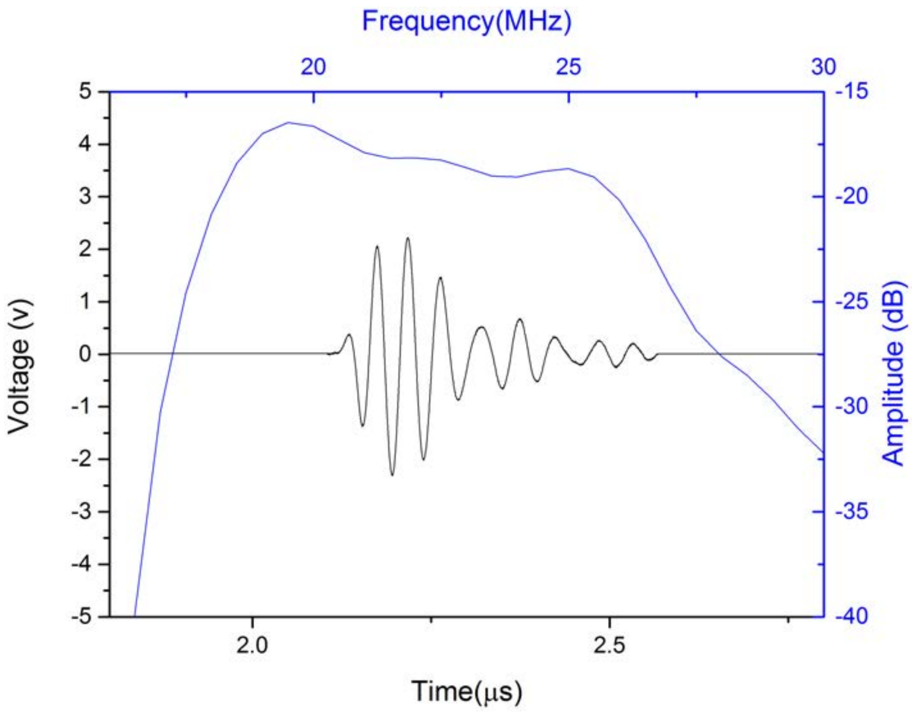

Figure 4.6 Array 1-Pulse echo waveform and frequency spectrum of a representative element.

Table 4.5 Array 1-Measured and simulated results in the pulse-echo waveform and frequency spectrum of a representative element

	Measured	Simulated
Center frequency f_c (MHz)	22.00	21.70
Peak to peak voltage (V)	4.2 (26 dB gain)	11.3×10^{-3} (No gain)
f_L (MHz)	26.48	13.24
f_H (MHz)	17.50	30.16
-6 dB Bandwidth (%)	41	78

Actually, the successful rate of the Array 1 is critically low due to the issue of connection between the array and coaxial cable. Only 30% elements had signals and the rest of them were disconnected or short circuited. The separations between the element electrodes were only 200 μm and the cables soldering were manipulated by hands under an optical microscope, so the successful rate becomes incredibly low. By checking the conductivity between the coaxial cables and the outer electrodes using a multimeter, the connections showed the excellent conductivity. However, the array showed a very low conductivity of electrode traces across the array and outer electrode traces. It was found that the gap between the ceramic base and the piezoelectric element is large such that the electrodes were separated as shown in Figure 4.7. The possible reason is that the adhesion of Cr/Au electrode on the gap was weak because the gap was filled by the epoxy. Furthermore, the surface of epoxy filled in the gap, the ceramic base and the array were not at the same elevation level. The thickness of the sputtered Au electrodes was unable to overcome the elevation difference that may be possible to cause the electrodes disconnection. Moreover, the Cr/Au electrode at the edge of the ceramic could be easily removed during the Cr/Au etching process. Thus, the connection method was changed for the second array (Array 2).

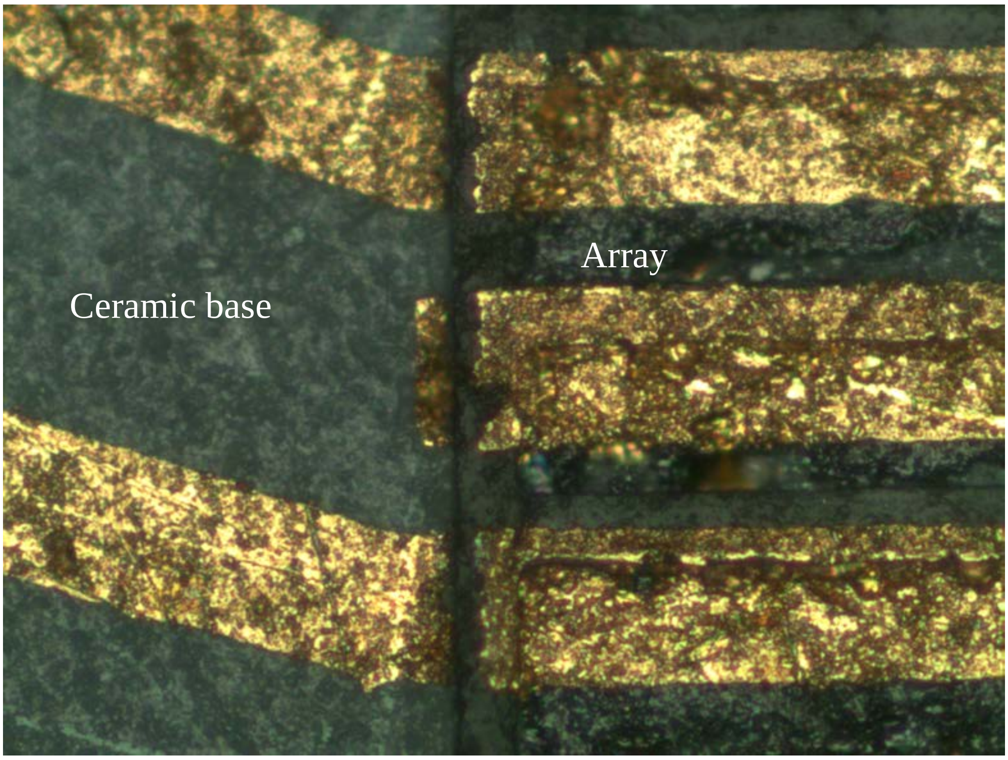

Figure 4.7 Array 2-The electrode traces separated across the ceramic base.

4.2 ARRAY 2

4.2.1 Design and fabrication

Based on the experience of Array 1, the electrical connection method was changed to achieve higher successful rate. A designed flexible circuit was used to connect the elements rather than using the coaxial cables connecting the elements one by one. The traces separation of flexible circuit was designed to be exactly the same as the electrodes separation of the array. The flexible circuit was aligned with the outer

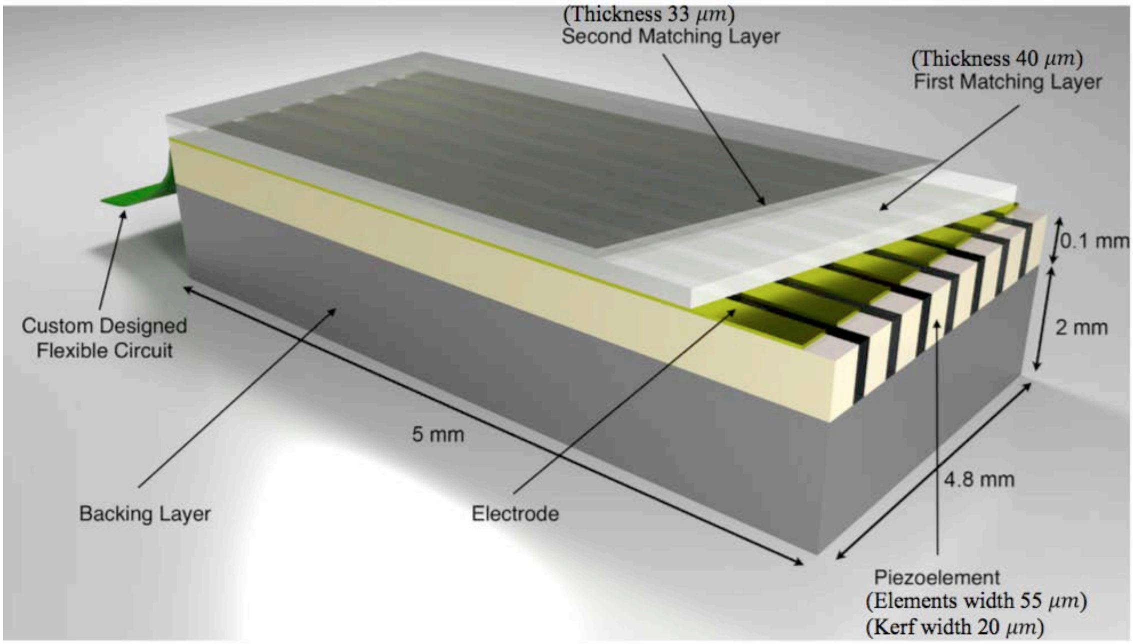

Figure 4.8 Schematic of Array 2 [54].

electrodes under the optical microscope, then pressed on the electrodes with a low-viscosity epoxy, M-bond 601 (Micro-Measurements), using a fixture. The other fabrication procedures were the same as Array 1. The last procedure was to cast the double matching layer on the array's front surface using the fixture and Epoxy 301. The schematic of Array 2 is illustrated in Figure 4.8 [54] and the fabricated phased-array prototype is shown in Figure 4.9.

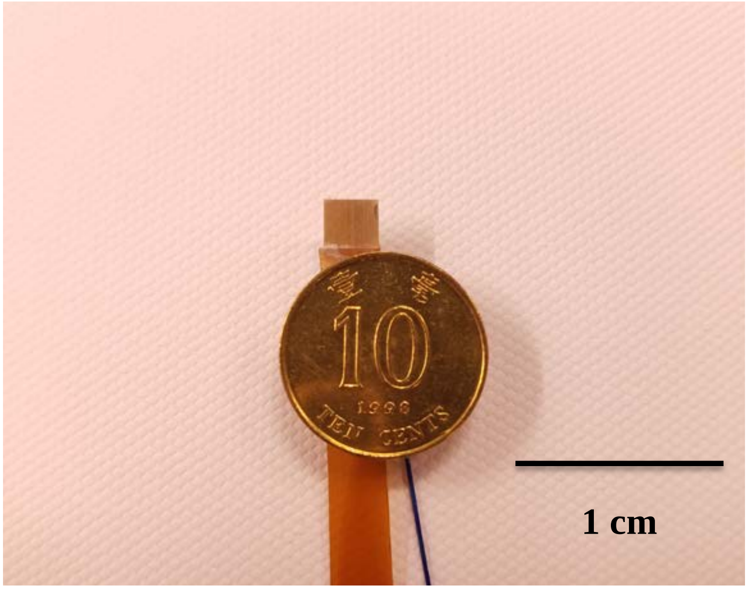

Figure 4.9 Photo of the fabricated Array 2 prototype.

4.2.2 Characterization

Figure 4.10 shows the electrical impedance and phase angle responses of a representative element while Table 4.6 shows the measured parameters. It is shown that three peaks appeared in the phase angle curve. The frequencies of the peaks were found to be 18.6 MHz, 12.2 MHz and 26.9 MHz, respectively. The peak at 18.6 MHz showed the largest phased angle shift and the values of other two peaks were remarkably small. Compared to the transition peaks (14 MHz, 22 MHz and 29 MHz) in Figure 4.1, the measured peaks of Array 2 were slightly shifted to lower frequencies. This may be

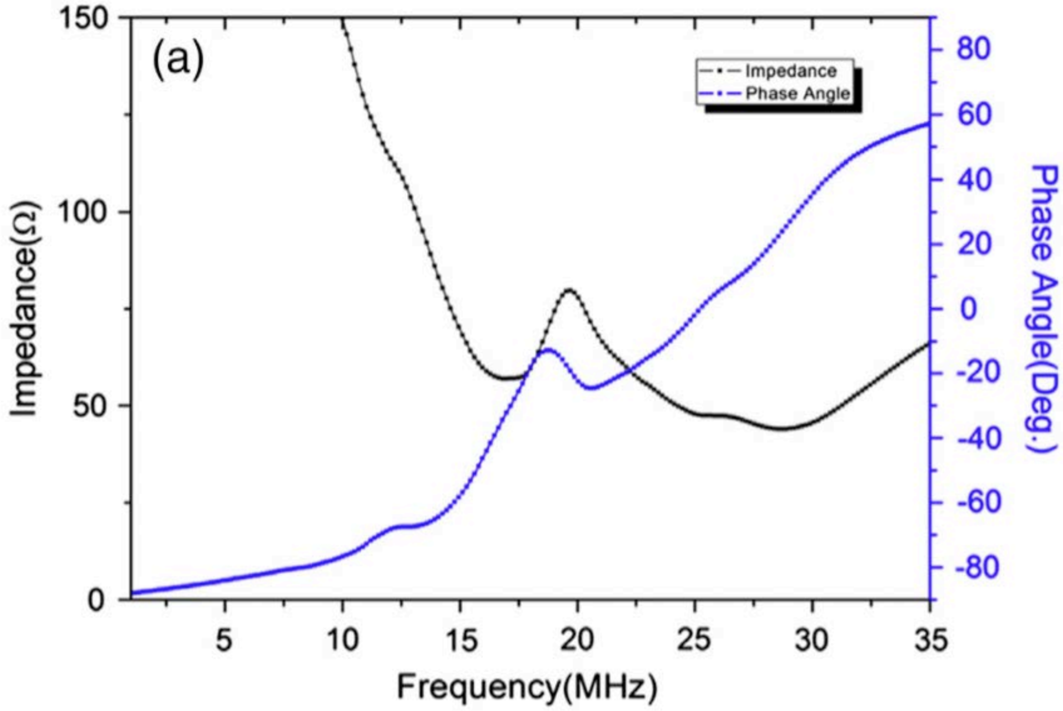

Figure 4.10 Array 2-Measured electrical impedance (black line) and phase angle (blue line) of a representative element.

attributed to the thickness variant during the lapping procedure. The flexible circuit was an extra electrical path in which the actual effect of electrical response on each element could not be estimated, although the effect could be added in the simulation or eliminated by doing the calibration of the impedance analyzer [32].

The simulated results are also listed in Tables 4.7. The impedance of Array 2 was 77.9 Ω @ 20 MHz, which was closer to the standard impedance requirement (50 Ω) than the simulated one. Thus, the energy transmission between the operation system and the array may be higher and the sensitivity of the array may also be enhanced.

Table 4.6 Array 2-Comparison of simulated and measured electrical properties of a representative element.

	Measured	Simulated
Peak of phased angle, f_p (MHz)	18.6	22.0
Impedance (Ω)	77.9 @ 20 MHz	101 @ 20 MHz
Resonance frequency, f_r (MHz)	17.2	19.0
Anti-resonance frequency, f_a (MHz)	19.7	25.0
Effective coupling coefficient, k_{eff}	0.53	0.69

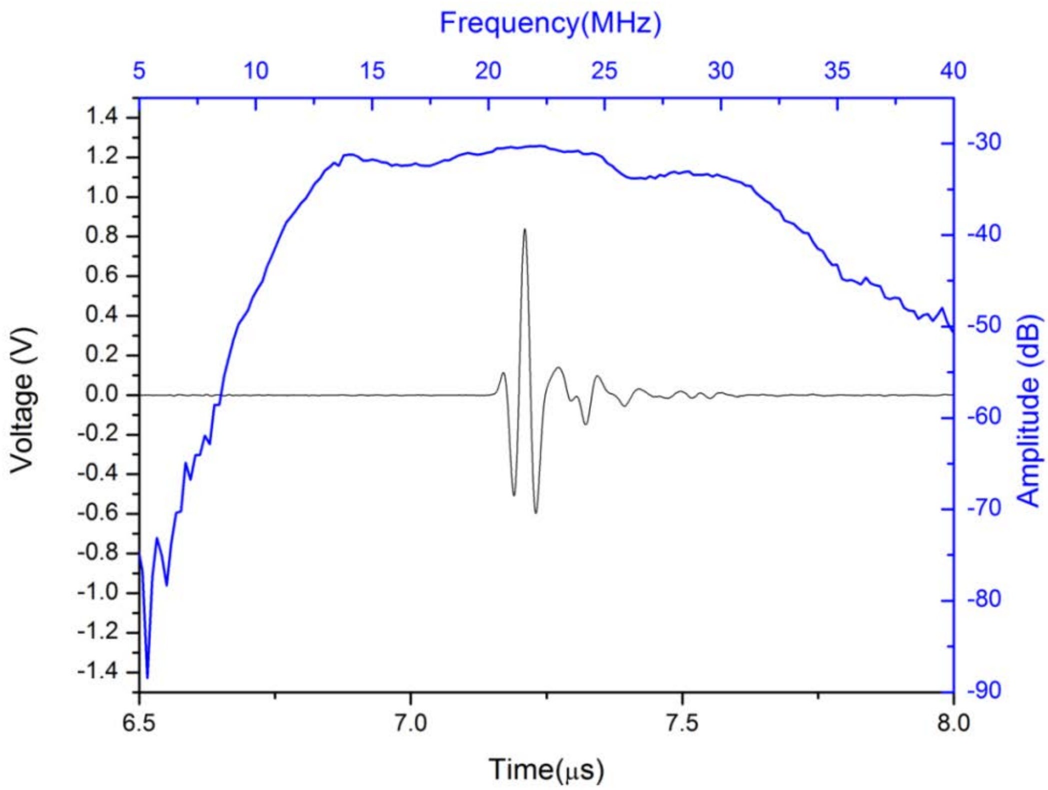

Figure 4.11 Array 2-Pulse-echo waveform and frequency spectrum of a representative element.

Figure 4.11 shows the pulse-echo waveform and frequency spectrum of a representative element of Array 2. Table 4.7 shows the measured results and compared with the simulated acoustic responses. Array 2 was shown to exhibit a -6 dB bandwidth of 91% with a frequency range from 12 MHz to 32 MHz. The bandwidth was extremely boarder than the simulated value and the reported results [31]-[34], [43].

Table 4.7 Comparison of simulated and measured properties of a representative element.

	Measured	Simulated
Center frequency, f_c (MHz)	22.0	21.7
Peak to peak voltage (V)	1.4 (26 dB gain)	11.3×10^{-3} (No Gain)
-6dB Bandwidth (%)	91	78
Pulse length (ns)	320	314
Insertion loss (dB)	29	N/A

The peak-to-peak value was 1.4 V with 26 dB gain received by the pulser/receiver. The pulse length of the array was 314 ns. The *IL* of the array was measured as 29 dB. The simulated (21.7 MHz) and measured (22.0 MHz) center frequencies agree well, resulting in the difference of only 0.3 MHz. The frequency discrepancy may be caused by the thickness variant in each layer. Table 4.8 illustrates the dimensions of the fabricated and the designed arrays. The thickness of the piezo-layer was 70 μm, which was thinner that the designed value (80 μm). The thicknesses of the inner and outer matching layers were thinner than the expected values as well, so this also caused the center frequency shifted to a higher value. Nevertheless, the discrepancy is small that can be neglected. The sensitivity of the fabricated array (an insertion loss of 29 dB) was higher than the simulated value (an insertion loss of ~40 dB). It may be attributed by the lower electrical impedance of the fabricated array. The impedance was closer to 50 Ω such that the energy transition should be better between the operation system and the array, resulting in more energy for acoustic pulse emission.

Table 4.8 Array 2-Designed and fabricated results in the pulse-echo waveform and frequency spectrum of a representative piezo-element.

	Designed	Fabricated
Piezo-elements thickness	80 μm	70 μm
Inner matching layer thickness	40 μm	38 μm
Outer matching layer thickness	33 μm	30 μm
Backing layer thickness	2 mm	2 mm
Kerf width	20 μm	23 μm
Piezo-element width	55 μm	52 μm

The most attractive result was the significantly bandwidth enhancement. The -6 dB bandwidth was 91% that was 10% wider than the simulated result. This may be attributed to the piezoelectric nature. From Table 4.8, the cutting kerf (22 μm) was wider than the designed one (20 μm), but the photolithographed electrodes remained at 55 μm, so the active layer became a 2-2 composite rather than a pure bulk single crystal. The acoustic impedance of 2-2 composite was lower than that of the bulk material according to the investigation of Wang *et al.* at 2013 [58]. Besides, the thickness mode electromechanical coupling coefficient of the 2-2 composite (≥ 0.6) is higher than that of the bulk material (0.5) if the crystal volume fraction of the composite is larger than 0.1 [59]. The piezo-elements with lower impedance would have a better impedance matching with the double matching layers, causing better transmission at high and low frequency ranges and wider bandwidth.

The fabricated array was found to have 50% bandwidth enhancement when comparing with the reported transducers fabricated using piezoelectric ceramics or ceramic-polymer composite materials. The comparisons are illustrated in Table 4.9 [31]-[34], [43]. The bandwidth of the phased-array transducer in this study was 10% wider than the linear-array transducer fabricated by Foster *et al.* (a -6 dB bandwidth of 80%). Theoretically, the phased-array transducer should have the highest axial resolution. However, the fabricated transducer exhibited a higher *IL* (29 dB) than that of the linear-array transducer (25 dB). The sensitivity of the fabricated transducer may be lower. The echo with a longer path may not be detected by the transducer, causing shallower imaging depth and lower resolution particularly for objects far from the transducer. Nevertheless, the *IL* was still in the acceptable range because images were still reported to acquire using the array transducer with an insertion loss of 46.4 dB [34]. According to Eqs. (3) and (4), the theoretical axial and lateral resolutions of Array 2 can be calculated as 37.46 μm and 16.04 μm at nf-ff distance, respectively. The axial and lateral resolutions are relatively high comparing with previous research. However, the calculation of lateral resolution does not consider the electronic beam formation, which can narrow the beam width depending on the number of elements and the focal length. The actual lateral resolution of the Array 2 should be significantly smaller than the calculated value.

Table 4.9 Comparisons of the reported transducers and Array 2.

	Array 2	**Linear-array fabricated by Nguyen-Dinh *et al. 1996* [34]**	**Phased-array fabricated by Chiu *et al.* 2014[33]**	**Phased-array fabricated by Bezanson *et al.* 2014 [43]**	**Linear-array fabricated by Stuart Foster *et al.* 2009 [31], [32]**
Designed center frequency	20 MHz	20 MHz	20 MHz	40 MHz	30 MHz
Material	PMN-30%PT	PZT-polymer composite	PZT-5H	PMN-32%PT	PZT-polymer composite
Number of element	64	128	48	64	256
Pitch	75 μm (1λ)	110 μm (~1.5 λ)	37 μm (~0.5λ)	38 μm (~1λ)	74 μm (~1.5λ)
-6 dB Bandwidth	91%	50%	61%	55%	80%
Insertion loss	29 dB	46.4 dB	N/A	N/A	25 dB

The fabricated transducer has shown an impressively wide bandwidth in the pulse-echo measurement, but the imaging performance of the transducer has not been evaluated yet. Moreover, the successful rate of the transducer was lower than 80% that was not enough for obtaining the medical imaging. Although the bandwidth was wide, the resolution of the transducer may still be affected by other factors, such as the side beam effect. The side beam effect was not observed in the pulse-echo measurement, but its effect is still unknown and may possibly affect the image acquisition. It is known that for a pitch lower than 0.5λ, the side beam effect can be totally neglected. To neglect the side beam effect, a transducer with the narrower pitch was highly desired to design and fabricate. On the other hand, the successful rate of was improved to higher than 80% for processing an image acquisition. The accomplishment of this work will be described in the next section.

4.3 ARRAY 3

4.3.1 Re-design the transducer with the narrower pitch

Array 2 has shown an accomplishment on wide bandwidth. For further performance improvement, a few modifications were taken on the latest array (Array 3). The side-beam effect has to be neglected as possible to minimize its adversely effect on imaging. The pitch of the array was narrowed from 75 μm (1λ) to 60 μm (0.8λ) that was closer to the ideal value (0.5 μm). In this case, the side-beam should appear at a larger angle. To remain the low electrical impedance of the array, the area of the elements should remain unchanged. Under this circumstance, the kerf was the only factor to be reduced. By using a new type of blade, which is called hub blade, the fluctuation of the blade during dicing can be reduced. The dicing kerf of the array was 20 μm when using a 15 μm thickness hub blade (ZH05-SD2000, DISCO, Japan).

Although the kerf width was narrower, the width of the elements was still reduced. However, even the impedance of the re-designed array is double (~300 Ω) that of Array 2, the impedance can still be coupled to 50 Ω by using the electrical coupling system. The second matching layer was replaced by Parylene C because it can be deposited to cover the whole transducer directly by using the Parylene C deposition system (Specialty Coating System, Inc., USA). Besides, the acoustic impedance of Parylene C (2.6 MRayls) was closer to the required acoustic impedance (2.3 MRayls) of second matching than the Epoxy 301 (3.0 MRayls). Thus, Parylene C should have a better impedance coupling. In addition to the low acoustic impedance, the waterproof and chemical proof features of Praylene C can also prevent the transducer from short-circuited by the water invading into the transducer, which could enhance the successful rate of the transducer. With the above changes, a new simulation result was modeled by PiezoCAD. The piezoelectric properties of the used PMN-0.3PT material and the properties of acoustic layers are listed in Table 4.10 and 4.11 respectively, and the simulated acoustic and electrical results are shown in Figures 4.12 and 4.13, respectively. All the dimensions of the new designed array are shown in Table 4.12, respectively.

Table 4.10 Measured piezoelectric properties of PMN-0.3PT bulk material used in Array 3

Material	PMN-0.3PT
Longitudinal velocity $\boldsymbol{v_z}$ **(ms^{-1})**	4038
Density $\boldsymbol{\rho}$ **(kgm^{-3})**	7920
Clamped dielectric constant $\boldsymbol{\varepsilon_{33}^{s}}$	621.6
Piezoelectric constant $\boldsymbol{d_{33}}$ **(pC/N)**	1400
Electromechanical coupling coefficient $\boldsymbol{k_t}$	0.58
Acoustic impedance $\boldsymbol{Z}$ **(MRayls)**	32
Thickness (μm)	500

Table 4.11 Array 3-Properties of acoustic layers.

Matching layer number	1	2	Backing layer
Material	$2-3\mu m$ Al_2O_3 powder + Epoxy 301	Parylene C	E-solder
Weight ratio	1.3:1	N/A	N/A
Acoustic impedance $(MRayls)$	7.6	2.6	5.9
Velocity (ms^{-1})	3320	2350	1850
Density (kgm^{-3})	2295	1100	3200

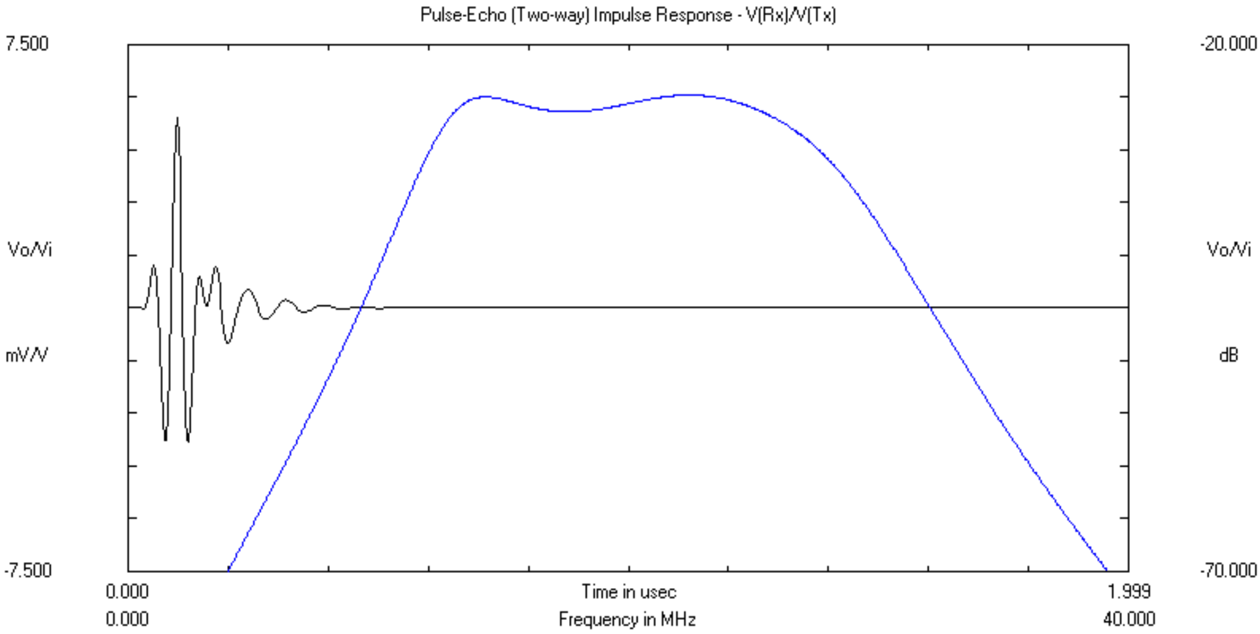

Figure 4.12 Array 3-Simulated pulse-echo (black) and frequency (blue) spectra.

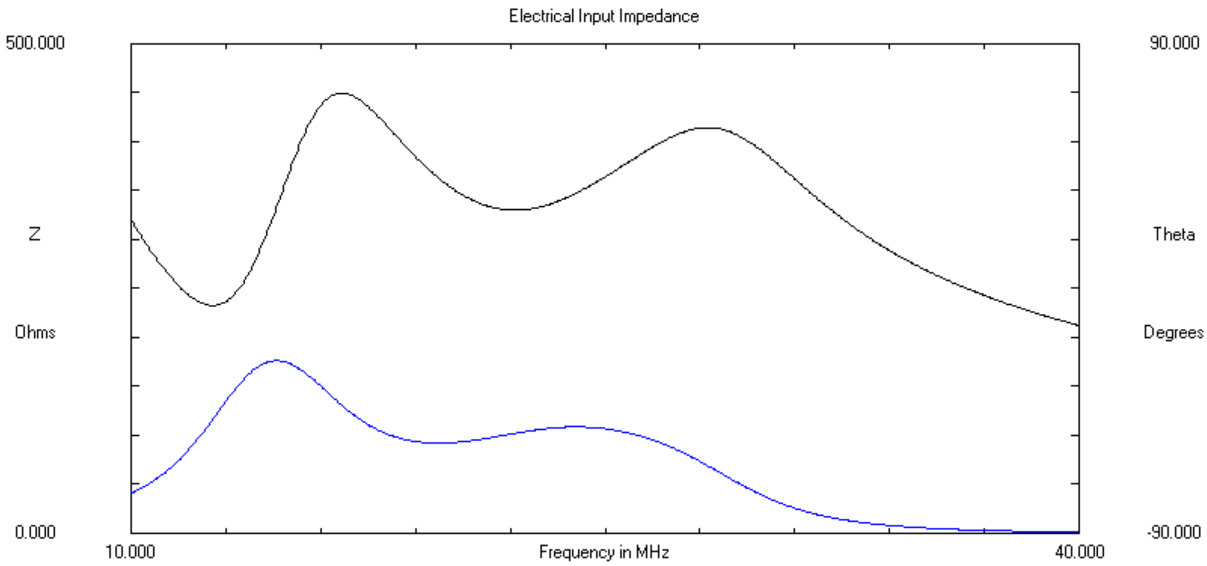

Figure 4.13 Array 3-Simulated electrical impedance (black) and phase angle (blue) spectra.

Table 4.12 Array 3-Specifications.

Designed center frequency	20 MHz
Number of elements	128
Pitch	60 μm (0.8λ)
Elements width	42 μm
Elements length	5 mm
Elevation dimension	2.16 mm
Azimuthal dimension	7.68 mm
Kerf width	18 μm
PMN-PT thickness	90 μm
First matching layer thickness	42 μm
Second matching layer thickness	28 μm
Backing layer thickness	2 mm

The simulated result showed a higher predicted -6dB bandwidth, which was 80.5%, comparing with the simulated result of Array 1. The peak-to-peak value was same as the previous simulation, and the center frequency was 19.9 MHz with an impedance of 367 Ω at 20 MHz. The high electrical impedance was caused by the low clamped dielectric constant of the PMN-0.3PT material. The simulated results fulfilled the requirement of wide bandwidth (>70 %), so the new design of the transducer might be feasible.

4.3.2 Fabrication process

Most of the fabrication processes were similar as the previous Array 1. The changed steps are listed as following:

1. Dice-and-fill process parameters: dicing separation ~ 60 μm (0.8λ pitch), a kerf of 20 μm, a cutting depth of 150 μm, and a dicing speed of 0.4 mm/s. The diced kerfs, shown in Figure 4.14, were captured by the built-in function of the dicing saw (DSD 3220, DISCO, Japan). The dicing index was selected to be 60 μm and all 128 elements were diced in one dicing process. This can reduce the fabrication time by bypassing one of the lapping processes.

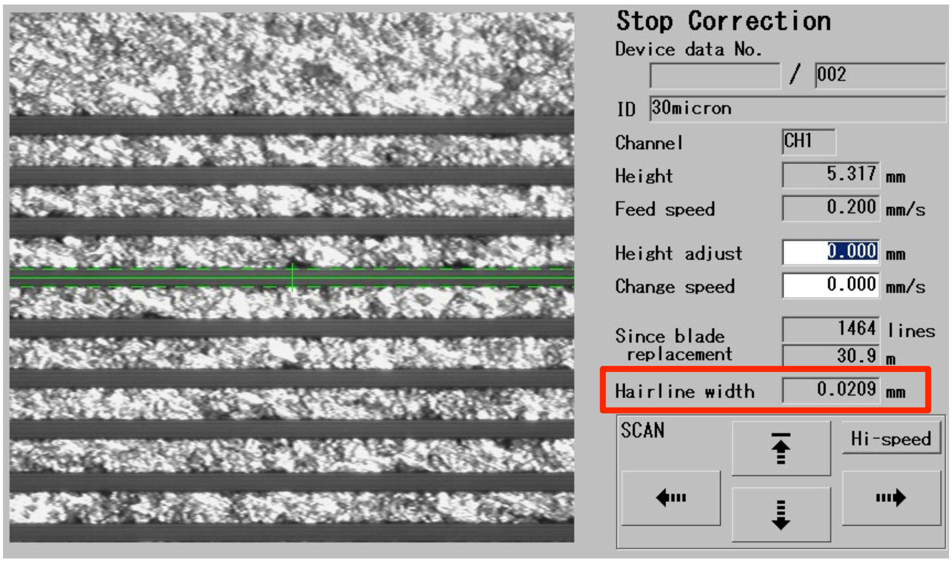

Figure 4.14 The profile of kerfs diced by the mechanical dicing saw.

2. Two custom designed flexible circuits with the trace separation double the array pitch were connected on both edges of the array by M-bond 610. The narrowest separation of the flexible circuit provided by the manufacturer is wider than the pitch of the array. Otherwise, the electrode traces of the flexible circuit would be shorted internally.

3. Only the first matching layer was casted on the front surface of the array. Then, a 28 μm-thick Parylene C was deposited on the array as the second matching layer.

4.3.3 Results and discussion

During the fabrication, some issues were found. The bulk PMN-0.3PT sample should have a thickness of >0.5 mm before the dicing process. The thinner sample would bend after the epoxy was filled, which was due to the thermal expansion difference between the epoxy and PMN-PT. The bending would influence the photolithography or sub-dicing alignment. It was found that the bending would not occur if the sample thickness was larger than 0.5 mm. Besides, the cutting depth and cutting speed were limited at 150 $\boldsymbol{\mu m}$ and 0.4 mm/s. The elements dropped off easily from the sample if the cutting depth is too large. Actually, this pitch ($\boldsymbol{60\ \mu m}$) reached the limitation of PMN-PT material by using the mechanical dicing method. Although the array was successfully fabricated, the failure rate was still high.

Compared to the previous array, the kerf width was narrower such that the air bubbles in the filled epoxy needed higher vacuum to remove thoroughly. The trapped bubbles would influence the Cr/Au etching process due to the sputtered Cr/Au on the bubbles

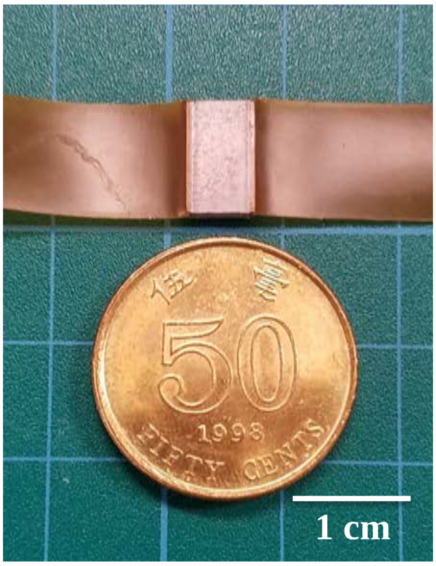

Figure 4.15 Top view of fabricated Array 3.

could not be etched. To prevent the electrodes short-circuited, re-dicing was replaced by the photolithography and etching processes. It enhanced the feasibility of the array development. The fabricated Array 3 transducer prototype is shown in Figure 4.15.

The insertion loss of all 128 elements have been investigated and shown in Figure 4.16.

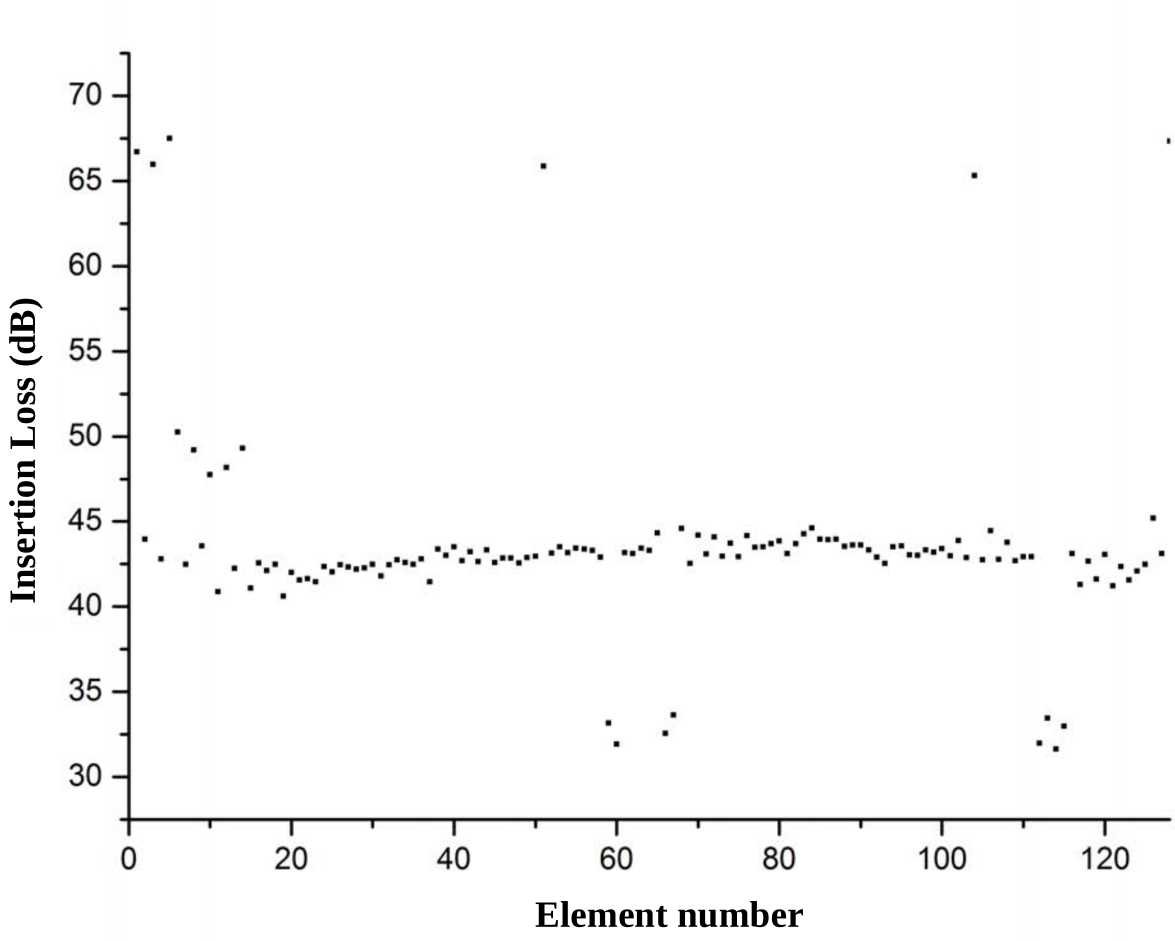

Figure 4.16 Array 3-Insertion loss of all 128 elements.

was higher than that of Array 2. 6 of 128 elements (elements #1, 3, 5, 51, 104 and 128) had much higher insertion loss than the average value, which indicate the disconnection feature of those elements. Besides, 8 of 128 elements (elements #59, 60, 66, 67, 112, 113, 114 and 115) were short-circuited with each other, which showed relatively low insertion loss compared to the average value. 5 of 128 elements (elements #6, 8, 10, 12 and 14) had slightly higher insertion loss than the average values, which was considered to be the weak-signal elements. According to the above observations, 109 of 128 elements had the insertion losses of around the average value, thus the successful rate was around 85%. The successful rate exceeded 80% (higher than the previous Array 2), which shows Array 3 fulfills the requirement of image acquisition.

For the electrical response, Figures 4.17 and 4.18 represent the electrical impedance-phase angle and capacitance-loss results of 109 of 128 elements, respectively. Both electrical responses show high uniformity among the elements under test. Table 4.13 shows that the impedance of a representative element was 401 Ω@20 MHz that is slightly higher than the simulated result, and the peak of the phase angle

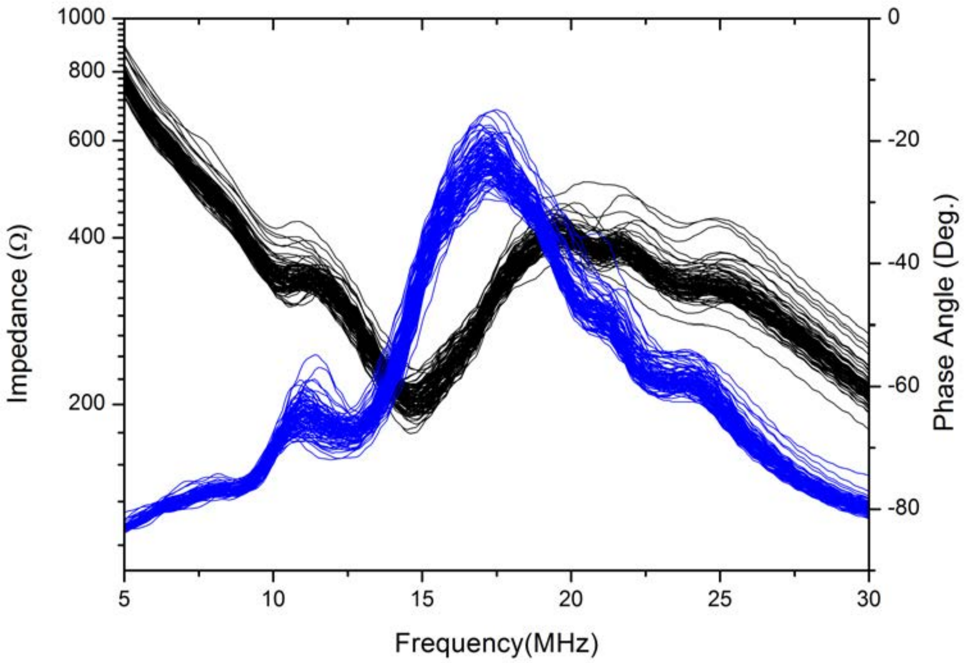

Figure 4.17 Array 3-Electrical impedance (black) and phased angle (blue) of 109/128 elements.

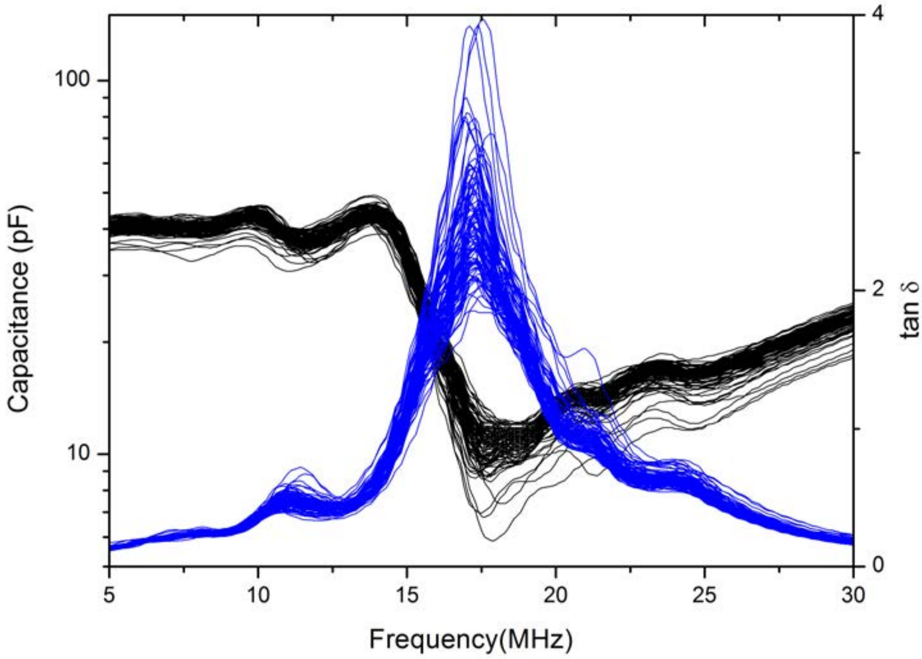

Figure 4.18 Array 3-Capacitance (black) and loss (blue) of 109 /128 elements.

was located at 17.2 MHz. Besides, the higher impedance was found because of the lower clamped dielectric constant and the narrower pitch of Array 3. It is known that the clamped dielectric constant is a parameter directly related to the electrical impedance of the transducer. On the other hand, the narrower pitch causes the smaller aperture size of each element. Thus, the electrical impedance is further increased in the latest array design. The phase angle peaks shifted to the lower frequency when compared to the simulated value, which may be due to the thickness variant of layers during the array development.

Table 4.13 Array 3-Measured electrical impedance and phase angle properties of a representative element.

Peak of phased angle f_p (MHz)	17.3
Impedance (Ω)	401@20 MHz
Resonance frequency f_r (MHz)	14.71
Anti-resonance frequency f_a (MHz)	19.57
Effective coupling coefficient k_{eff}	0.70

For the capacitance and the loss curves, the peak of the loss was located at 17.3 MHz. This frequency was possibly the center frequency of Array 3. The capacitance at 20 MHz was 13.22 pF that matched with the value calculated using the clamped dielectric constant and the aperture size of the element.

In Figure 4.19, the pulse-echo response of Array 3 showed an amplitude of 1.38 $V_{p\text{-}p}$ with a 26 dB gain, which is compatible with the performance of Array 2, although the electrical impedance of Array 3 was higher than that of Array 2.

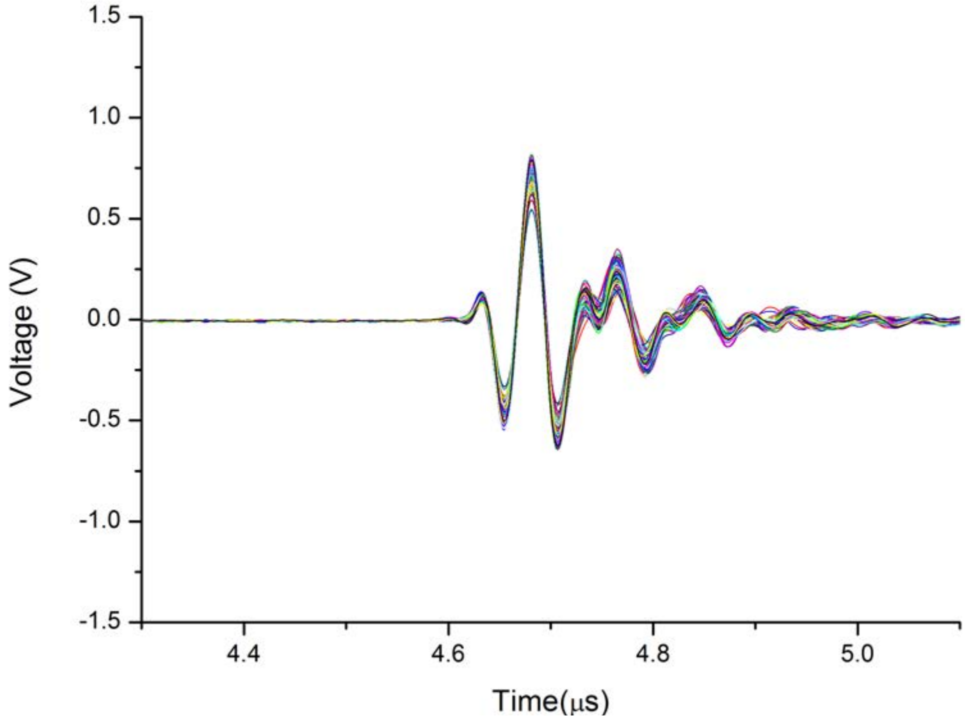

Figure 4.19 Array 3-Pulse-echo waveforms of 109/128 elements.

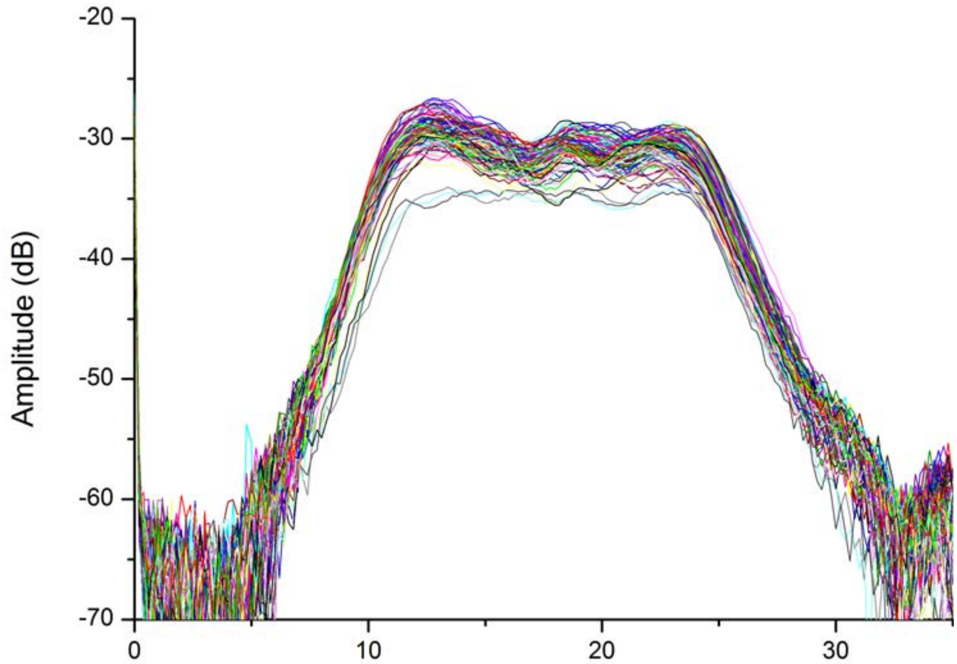

Figure 4.20 Array 3-Frequency response spectra of 109/128 elements.

Table 4.14 Array 3-Measured results in the pulse-echo waveform and frequency response spectrum of a representative element.

Center frequency f_c (MHz)	17.5
Peak to peak voltage (V)	1.38
f_L (MHz)	10.11
f_H (MHz)	24.98
-6dB Bandwidth (%)	84.8

Table 4.14 shows that the center frequency of Array 3 was 17.5 MHz calculated by the two -6 dB frequency points. The center frequency matched with the electrical response in which the highest phase angle peak was at 17.3 MHz. The lower center frequency was probably due to the thickness variant in different layers. The pulse-echo waveforms, as shown in Figure 4.19, show the appearance of ring-down after one pulse period and it repeated twice with the continuous decreasing amplitude. Referring to the backing layer, the acoustic impedance may not be high enough for full acoustic pulse transmission, furthermore, the absorption of backing still have to be improved for lower the ring-down phenomena. The backing layer can be replaced by a mixture of powder and epoxy to tune the acoustic impedance and absorption at the required frequency via

changing the particle size of the powder and the ratio of components. According to Section 1.2.3.4, the particle size can control the wave scattering and reflection at different frequencies, respectively. By using the powders with the required particle size, the absorption improvement of the back reflected pulse can be predicted so as to further widen the bandwidth of the transducer. As shown in Figure 4.20, the responses at frequency of around 11 MHz showed the highest acoustic response when compared with those at other frequencies. Nevertheless, the frequency response was still steady in the frequency range within 11 MHz to 25 MHz. Although there was the ring-down with Array 3, the -6 dB bandwidth still accomplished almost 85%, which is higher than that of the PZT array developed by Stuart Foster *et al.* at 2009 [31], [32]. The maximum bandwidth of Array 3 was not higher than the array fabricated by Jiang *et al.* at 2010, but the results of Array 3 showed a significantly high uniformity such that the average -6 dB bandwidth is higher. The axial and lateral resolutions of the Array 3 were calculated as 50.44 μm and 10.03 μm so that the axial resolution is comparable and the lateral resolution is slight higher than Array 2, respectively.

The crosstalks of adjacent elements (both left and right sides) and one element next to the adjacent element of the representative element located at #100 in the Array 3 are shown in Figure 4.21. The adjacent elements on both left and right sides have nearly exact the same crosstalk against the frequency. This feature can also be seen on the one next to the adjacent elements. The crosstalks of the adjacent elements were around -45 dB in the frequency range from 20 MHz to 37 MHz. The crosstalks were relative higher in the frequency range from 10 MHz to 20 MHz. The maximum crosstalk of -32 dB from the adjacent elements was located at around 15 MHz. The crosstalk of the one next to the adjacent elements had the similar trend of the adjacent elements, but the response

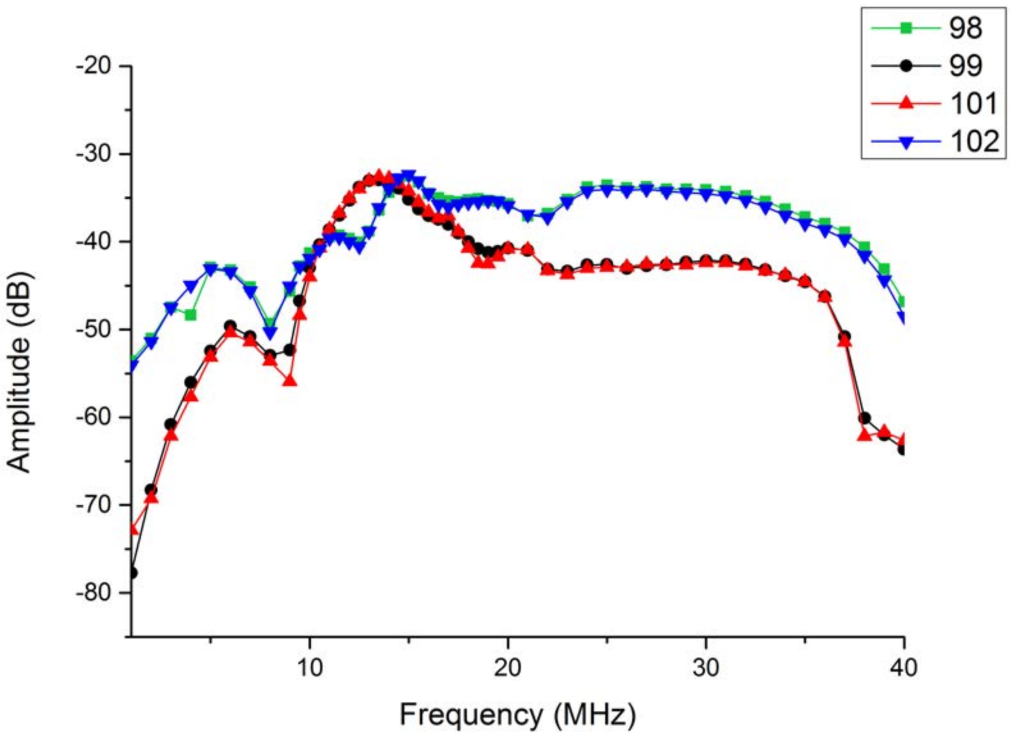

Figure 4.21 Array 3-Crosstalk of adjacent elements (left and right sides) and one more next to the adjacent elements (left and right) of element #100.

became flatter in the frequency range from 13 MHz to 40 MHz. Compared to the crosstalks of the adjacent elements, the crosstalks of the one next to the adjacent elements were higher that were around -35 dB. Guess *et al.* has reported the crosstalk feature of a 3-MHz array transducer in which the crosstalk of the next to the adjacent element had a -45 dB amplitude that was lower than that of the adjacent elements (-24 dB) [60]. The measured crosstalk trend in this study was completely opposite to the result reported by Guess *et al*. The possible explanation is that the even number of elements was connected with the same flexible circuit attached with the source elements. It may generate higher crosstalk through the electrodes of the flexible circuit, and this phenomena has been observed from the 35-MHz linear-array developed by Cannata *et al.* in 2006 [9]. The crosstalk of the fabricated Array 3 is comparable with the array transducers using the PZT material, although the crosstalk of Array 3 had higher crosstalk than the previous Array 2.

CHAPTER 5 CONCLUSION

In this study, three phased-array ultrasound transducers with high axial and lateral resolutions for biomedical imaging were studied. Table 5.1 summarizes the specifications of different arrays fabricated in this study. The accomplishments have been obtained by using the piezoelectric PMN-0.3PT single crystal material as the active layer of the 20-MHz transducer. A 64-element phased-array transducer has been successfully fabricated by the mechanical dicing method, which showed a very wide -6dB bandwidth of 91% and an insertion loss of 29 dB with a center frequency of 22 MHz, but with a lower than 80% successful rate that does not fulfill the requirement for medical imaging. Another 128-element phased-array transducer using the PMN-0.3PT material has presented a wide bandwidth of 85% at the center frequency of 17.5 MHz. The bandwidth was slightly lower than the previous Array 2, and the frequency was lower than our initial design. The sensitivity of Array 3 is relatively low compared to Array 2, which had an average insertion loss of -45 dB. However, the overall result of Array 3 was better than that of the reported PZT array transducers.

When comparing with other reported work and even the commercial array transducers, the fabricated phased-array transducer still has the widest bandwidth with a comparable sensitivity. The bandwidth of the fabricated Array 3 was 27% higher than that of the

20-MHz phased-array ultrasound transducer investigated by Chiu et al. [33], and ~34% higher than that of the 40-MHz phased-array developed by Bezanson et al. [59]. Theoretically, the wide -6 dB bandwidth is a direct evidence of high axial resolution, which means that the axial resolution of the fabricated 20-MHz PMN-PT phased-array should be higher than that of the other reported array transducers. The lateral resolution of the transducer depends on the beam width and the center frequency. By using the phased-array beam forming method with 128 elements at the center frequency of 17.5 MHz, the transducer fabricated in this study should have the comparable lateral resolution with other studies. Moreover, 85% (109/128) of elements of Array 3 worked properly with an impressively high uniformity in performance.

Table 5.1 Comparison of three different phased-array transducers.

	Array 1	Array 2	Array 3
First matching layer	N/A	Al_2O_3 powder + Epoxy 301	Al_2O_3 powder + Epoxy 301
Second matching layer	N/A	Epoxy 301	Parylene C
Backing layer	E-solder	E-solder	E-solder
Number of element	64	64	128
Pitch	75 μm ($\sim 1\lambda$)	75 μm ($\sim 1\lambda$)	60 μm ($\sim 0.8\lambda$)
Bandwidth	41%	91%	85%
Insertion loss	N/A	29 dB	45 dB
Percentage of good elements	<10%	~60%	~85%

Besides, the size of the transducer was ((L) 8 mm × (W) 5 mm × (H) 2.2 mm). Although it is not the smallest transducer and cannot be used for invasive imaging, it is still capable for small biomedical tissues imaging due to the features of high -6 dB bandwidth and high frequency.

CHAPTER 6 FUTURE WORK

The measurement of axial and lateral resolutions and biomedical imaging has not been achieved by using the phased-array transducers fabricated in this study. The following investigation will be practically to use the fabricated Array 3 to acquire wire phantom imaging to determinate its axial and lateral resolutions. Furthermore, biomedical tissue imaging will be performed by using Array 3.

The 20-MHz PMN-0.3PT phased-array has been successfully accomplished, however, 20 MHz is the minimum frequency in the high frequency range. The center frequency of the phased-array transducer will be further increased for achieving a higher lateral resolution. Other fabrication method will be investigated to overcome the limitation of mechanical dicing on the PMN-PT material.

REFERENCES

[1] D. H. Turnbull, "In Utero Ultrasound Backscatter Microscopy of Early Stage Mouse Embryos," *Computerized Medical Imaging and Graphics*, vol. 23, no. 1, pp. 25–31, 1999.

[2] G. R. Lockwood, D. H. Turnball, D. A. Christopher, and F. S. Foster, "Beyond 30 MHz [Applications of High-Frequency Ultrasound Imaging]," *Engineering in Medicine and Biology Magazine, IEEE*, vol. 15, no. 6, pp. 60–71, 1996.

[3] F. S. Foster, G. R. Lockwood, L. K. Ryan, K. A. Harasiewicz, and L. Berube, "Principles and Applications of Ultrasound Backscatter Microscopy," *IEEE Trans. Ultrason., Ferroelect., Freq. Contr.*, vol. 40, no. 5, pp. 608–617, 1993.

[4] C. Passmann and H. Ermert, "A 100-MHz Ultrasound Imaging System for Dermatologic and Ophthalmologic Diagnostics," *IEEE Trans. Ultrason., Ferroelect., Freq. Contr.*, vol. 43, no. 4, pp. 545–552, Jul. 1996.

[5] P. Hoskins, K. Martin, and A. Thrush, *Diagnostic Ultrasound*, 2nd ed. 2010, pp. 1–276.

[6] "Vevo® 3100 - High-Frequency Ultrasound Imaging for Preclinical Research | VisualSonics," *visualsonics.com*. [Online]. Available: http://www.visualsonics.com/products/vevo-3100. [Accessed: 09-Dec-2016].

[7] J. S. Mattoon and T. G. Nyland, *Small Animal Diagnostic Ultrasound*. Elsevier Health Sciences, 2014.

[8] K. K. Shung, *Diagnostic Ultrasound*. CRC Press, 2015.

[9] J. M. Cannata, J. A. Williams, Q. F. Zhou, T. A. Ritter, and K. K. Shung, "Development of a 35-MHz Piezo-Composite Ultrasound Array for Medical Imaging," *IEEE Trans. Ultrason., Ferroelect., Freq. Contr.*, vol. 53, no. 1, pp. 224–236, Jan. 2006.

[10] E. Lacaze, S. Michau, and P. Mauchamp, "20 MHz Ultrasound Array for Medical Imaging From Design to Image Evaluation," presented at the 2001 IEEE Ultrasonics Symposium. Proceedings. An International Symposium, 2001, vol. 2, pp. 1139–1142.

[11] W. Qiu, Y. Chen, C.-M. Wong, B. Liu, J. Dai, and H. Zheng, "A Novel Dual-Frequency Imaging Method for Intravascular Ultrasound Applications," *Ultrasonics*, vol. 57, no. C, pp. 31–35, Mar. 2015.

[12] N. Kovacevic, "A Three-dimensional MRI Atlas of the Mouse Brain with Estimates of the Average and Variability," *Cerebral Cortex*, vol. 15, no. 5, pp. 639–645, Sep. 2004.

[13] O. Catherine and M. Otto, *Textbook of Clinical Echocardiography*. 2000.

[14] C. R. Bowen, H. A. Kim, P. M. Weaver, and S. Dunn, "Piezoelectric and Ferroelectric Materials and Structures for Energy Harvesting Applications," *Energy Environ. Sci.*, vol. 7, no. 1, pp. 25–44, 2014.

[15] Jie Chen and R. Panda, "Review: Commercialization of Piezoelectric Single Crystals for Medical Imaging Applications," presented at the IEEE Ultrasonics Symposium, 2005., 2005, vol. 1, pp. 235–240.

[16] B. A. J. Angelsen, *Ultrasound imaging : Waves, Signals, and Signal Processing*, 2nd ed. Emantec, 2000.

[17] C. S. Desilets, "Transducer Arrays Suitable for Acoustic Imaging," Ph.D. Thesis Stanford Univ., 1978.

[18] Y. Qian and N. R. Harris, "Modelling of a Novel High-Impedance Matching Layer for High Frequency (>30MHz) Ultrasonic Transducers," *Ultrasonics*, vol. 54, no. 2, pp. 586–591, Feb. 2014.

[19] H. W. PERSSON and C. H. HERTZ, "Acoustic-Impedance Matching of Medical Ultrasound Transducers," *Ultrasonics*, vol. 23, no. 2, pp. 83–89, 1985.

[20] R. Chen, N. E. Cabrera-Munoz, K. H. Lam, H. S. Hsu, F. Zheng, Q. Zhou, and K. K. Shung, "PMN-PT Single-Crystal High-Frequency Kerfless Phased Array," *IEEE Trans. Ultrason., Ferroelect., Freq. Contr.*, vol. 61, no. 6, pp. 1033–1041, May 2014.

[21] C. E. Morton and G. R. Lockwood, "Evaluation of Kerfless Linear Arrays," presented at the 2002 IEEE International Ultrasonics Symposium, 2002, vol. 2, pp. 1257–1260.

[22] J. M. Cannata, J. A. Williams, and K. K. Shung, "A Kerfless 30 MHz Linear Ultrasonic Array," *Ultrasonics Symposium, 2005 IEEE*, vol. 1, pp. 109–112, 2005.

[23] B. Zhu, N. Y. Chan, J. Dai, K. K. Shung, S. Takeuchi, and Q. Zhou, "New Fabrication of High-Frequency (100-MHz) Ultrasound PZT Film Kerfless Linear Array," *IEEE Trans. Ultrason., Ferroelect., Freq. Contr.*, vol. 60, no. 4, pp. 854–857, Apr. 2013.

[24] B. P. Zhu, D. W. Wu, Y. Zhang, J. Ou-Yang, S. Chen, and X. F. Yang, "Sol-Gel Derived PMN-PT Thick Films for High Frequency Ultrasound Linear Array Applications," *Ceramics International*, vol. 39, no. 8, pp. 8709–8714, Dec. 2013.

[25] G. G. Harman, *Wire Bonding in Microelectronics; 3rd Ed.* New York, NY: McGraw-Hill, 2010.

[26] H. Li, "Fabrication of Single Crystal Based Phased Array Medical Imaging

Ultrasonic Transducers," 2008.

[27] J. Kuwata, K. Uchino, and S. Nomura, "Dielectric and Piezoelectric Properties of $0.91Pb(Zn_{1/3}Nb_{2/3})O_3$-$0.09PbTiO_3$ Single Crystals," *Jpn. J. Appl. Phys.*, vol. 21, no. 9, pp. 1298–1302, Sep. 1982.

[28] H. Li, Y. C. Li, D. Zhou, J. Peng, H. S. Luo, and J. Y. Dai, "Application of PMNPT Single Crystal in a 3.2 MHz Phased-Array Ultrasonic Medical Imaging Transducer," presented at the 2007 Sixteenth IEEE International Symposium on the Applications of Ferroelectrics, 2007, pp. 572–574.

[29] K. H. Lam, Y. Chen, K. F. Cheung, and J. Y. Dai, "PMN–PT Single Crystal Focusing Transducer Fabricated Using a Mechanical Dimpling Technique," *Ultrasonics*, vol. 52, no. 1, pp. 20–24, Jan. 2012.

[30] C. G. Oakley and M. J. Zipparo, "Single Crystal Piezoelectrics: a Revolutionary Development for Transducers," *IEEE 1992 Ultrasonics Symposium Proceedings*, vol. 2, pp. 1157–1167, 2000.

[31] F. S. Foster, J. Mehi, M. Lukacs, D. Hirson, C. White, C. Chaggares, and A. Needles, "A New 15-50 MHz Array-Based Micro-Ultrasound Scanner for Preclinical Imaging," *Ultrasound in Medicine & Biology*, vol. 35, no. 10, pp. 1700–1708, Oct. 2009.

[32] M. Lukacs, J. Yin, G. Pang, R. Garcia, E. Cherin, R. Williams, J. Mehi, and F. Foster, "Performance and Characterization of New Micromachined High-Frequency Linear Arrays," *IEEE Trans. Ultrason., Ferroelect., Freq. Contr.*, vol. 53, no. 10, pp. 1719–1729, Sep. 2006.

[33] C. T. Chiu, J. A. Williams, B. J. Kang, T. Abraham, K. K. Shung, and H. H. Kim, "Fabrication and Characterization of a 20 MHz Microlinear Phased Array Transducer for Intervention Guidance," presented at the 2014 IEEE International Ultrasonics Symposium, 2014, pp. 2121–2124.

[34] A. Nguyen-Dinh, L. Ratsimandresy, P. Mauchamp, R. Dufait, A. Flesch, and M. Lethiecq, "High Frequency Piezo-Composite Transducer Array Designed for Ultrasound Scanning Applications," presented at the 1996 IEEE Ultrasonics Symposium. Proceedings, 1996, vol. 2, pp. 943–947.

[35] X. Jiang, K. Snook, R. Liu, X. Geng, and W. S. Hackenberger, "Fabrication and Characterization of High Frequency Phased Arrays for NDE Imaging," *Proceedings of the SPIE*, vol. 7649, p. 76490X, Apr. 2010.

[36] P. Sun, Q. Zhou, B. Zhu, D. Wu, C. Hu, J. M. Cannata, J. Tian, P. Han, G. Wang, and K. K. Shung, "Design and Fabrication of PIN-PMN-PT Single-Crystal High-Frequency Ultrasound Transducers," *IEEE Trans. Ultrason., Ferroelect., Freq. Contr.*, vol. 56, no. 12, pp. 2760–2763, Dec. 2009.

[37] H. J. Hwang, T. Nagai, T. Ohji, M. Sando, M. Toriyama, and K. Niihara, “Curie Temperature Anomaly in Lead Zirconate Titanate/Silver Composites,” *J American Ceramic Society*, vol. 81, no. 3, pp. 709–712, Mar. 1998.

[38] K. H. Lam, H. F. Ji, F. Zheng, W. Ren, Q. Zhou, and K. K. Shung, “Development of Lead-Free Single-Element Ultrahigh Frequency (170-320 MHz) Ultrasonic Transducers,” *Ultrasonics*, vol. 53, no. 5, pp. 1033–1038, Jul. 2013.

[39] L. Zhang, X. Xu, C. Hu, L. Sun, J. T. Yen, J. M. Cannata, and K. K. Shung, “A High-Frequency, High Frame Rate Duplex Ultrasound Linear Array Imaging System for Small Animal Imaging,” *IEEE Trans. Ultrason., Ferroelect., Freq. Contr.*, vol. 57, no. 7, pp. 1548–1557, Jul. 2010.

[40] J. Powers and F. Kremkau, “Medical Ultrasound Systems,” *Interface Focus*, vol. 1, no. 4, pp. 477–489, 2011.

[41] “Ultrasonic probe (Transducer) / NDK,” *ndk.com*. [Online]. Available: http://www.ndk.com/en/products/search/ultrasonic/. [Accessed: 05-Dec-2016].

[42] M. Cannata, Q. F. Zhou, and K. K. Shung, “Development of a High Frequency (35 MHz) Linear Ultrasonic Array Using 2-2 Composite Elements [Biomedical Applications],” *IEEE 1992 Ultrasonics Symposium Proceedings*, vol. 2, pp. 894–897 Vol.2, 2004.

[43] A. Bezanson, R. Adamson, and J. A. Brown, “Fabrication and Performance of a Miniaturized 64-Element High-Frequency Endoscopic Phased Array,” *IEEE transactions on …*, vol. 61, no. 1, pp. 33–43, Jan. 2014.

[44] Y. Ito, K. Kushida, K. Sugawara, and H. Takeuchi, “A 100-MHz Ultrasonic Transducer Array Using ZnO Thin Films,” *IEEE Trans. Ultrason., Ferroelect., Freq. Contr.*, vol. 42, no. 2, pp. 316–324, Mar. 1995.

[45] J. M. Cannata, T. A. Ritter, and K. K. Shung, “A 35 MHz Linear Array for Medical Imaging,” presented at the 2001 IEEE Ultrasonics Symposium. Proceedings. An International Symposium, 2001, vol. 2, pp. 1157–1160.

[46] H. P. Savakus, K. A. Klicker, and R. E. Newnham, “PZT-Epoxy Piezoelectric Transducers: a Simplified Fabrication Procedure,” *Materials Research Bulletin*, vol. 16, no. 6, pp. 677–680, Jun. 1981.

[47] A. R. Selfridge, “The Design and Fabrication of Ultrasonic Transducers and Transducer Arrays,” Stanford University, 1982.

[48] Changgeng Liu, Qifa Zhou, F. T. Djuth, and K. K. Shung, “High-Frequency (>50 MHz) Medical Ultrasound Linear Arrays Fabricated From Micromachined Bulk PZT Materials,” *IEEE Trans. Ultrason., Ferroelect., Freq. Contr.*, vol. 59, no. 2, pp. 315–318, 2012.

[49] R. Krimholtz, D. A. Leedom, and G. L. Matthaei, “New Equivalent Circuits for Elementary Piezoelectric Transducers,” *Electron. Lett.*, vol. 6, no. 13, p. 398, 1970.

[50] S. Sherrit, S. P. Leary, B. P. Dolgin, and Y. Bar-Cohen, “Comparison of the Mason and KLM Equivalent Circuits for Piezoelectric Resonators in the Thickness Mode,” *ULTSYM-99*, vol. 2, pp. 921–926, 1999.

[51] W. Sriratana, R. Murayama, and L. Tanachaikhan, “Synthesis and Analysis of PZT Using Impedance Method of Reactance Estimation,” *AMPC*, vol. 3, no. 1, pp. 62–70, 2013.

[52] “Equine Ultrasound Therapy – EQultrasound » Ultrasound Therapy 2.0,” *equltrasound.com*. [Online]. Available: http://www.equltrasound.com/general-info-about-therapeutic-ultrasound/. [Accessed: 08-Dec-2016].

[53] S. T. Lau, H. Li, K. S. Wong, Q. F. Zhou, D. Zhou, Y. C. Li, H. S. Luo, K. K. Shung, and J. Y. Dai, “Multiple Matching Scheme for Broadband $0.72Pb(Mg_{1/3}Nb_{2/3})O_3$-$0.28PbTiO_3$ Single Crystal Phased-Array Transducer,” *J. Appl. Phys.*, vol. 105, no. 9, p. 4908, May 2009.

[54] C.-M. Wong, Y. Chen, H. Luo, J. Dai, K. H. Lam, and H. L.-W. Chan, “Development of a 20-MHz Wide-Bandwidth PMN-PT Single Crystal Phased-Array Ultrasound Transducer,” *Ultrasonics*, vol. 73, no. C, pp. 181–186, Jan. 2017.

[55] T. A. Ritter, K. K. Shung, X. Geng, P. D. Lopath, R. L. Tutwiler, and T. R. Shrout, “Composite Ultrasound Transducer Arrays for Operation Above 20 MHz,” presented at the Proceedings of the SPIE, 1999, vol. 3664, pp. 67–75.

[56] J. M. Cannata, T. A. Ritter, and W. H. Chen, “Design of Efficient, Broadband Single-Element (20-80 MHz) Ultrasonic Transducers for Medical Imaging Applications,” *IEEE Trans. Ultrason., Ferroelect., Freq. Contr.*, vol. 50, no. 11, pp. 1548–1557, 2003.

[57] S. Saitoh, T. Takeuchi, and T. Kobayashi, “A 3.7 MHz Phased Array Probe Using 0.91 Pb $(Zn_{1/3} Nb_{2/3}) O_3$ -0.09 $PbTiO_3$,” *IEEE transactions on …*, vol. 46, no. 2, pp. 414–421, 1998.

[58] W. Wang, S. W. Or, Q. Yue, Y. Zhang, J. Jiao, C. M. Leung, X. Zhao, and H. Luo, “Ternary Piezoelectric Single-Crystal PIMNT Based 2-2 Composite for Ultrasonic Transducer Applications,” *Sensors & Actuators: A. Physical*, vol. 196, pp. 70–77, Jul. 2013.

[59] W. K. Qi and W. W. Cao, “Finite Element Analysis and Experimental Studies on the Thickness Resonance of Piezocomposite Transducers,” *Ultrasonic*

Imaging, vol. 18, no. 1, pp. 1–9, Jan. 1996.

[60] J. F. Guess, C. G. Oakley, S. J. Douglas, and R. D. Morgan, "Cross-Talk Paths in Array Transducers ," presented at the 1995 IEEE Ultrasonics Symposium. An International Symposium, 1995, vol. 2, pp. 1279–1282.